

Sandia flame D

Solution sensitivity to the combustion mechanism

Abstract

A number of chemical reaction mechanisms is tested against the well-known Sandia flame D case to assess their respective accuracy degree and computational cost.

Marco Talice
m.talicee@pm2engineering.com

Sandia flame D

Solution sensitivity to the combustion mechanism

Author: Marco Talice

Date: 10/04/2023

Version 1: comparison of reaction mechanisms

Date: 24/04/2023

Version 2: added 1-step results w/ RSM model

Date: 24/04/2023

Version 3: added comparison of RSM - 1-step results w/ and w/o inlet velocity profile

Date: 01/05/2023

Version 4: added comparison of RSM – gri3.0 vs RSM – gri2.11

Contents

Test case.....	3
Computational Domain and Mesh.....	3
Boundary Conditions.....	3
OpenFoam settings and miscellaneous	3
Tested reaction's mechanisms.....	3
Results.....	5
Tables	5
Convergence	7
Color fields	7
Temperature	8
Flame front.....	9
XY-plots	10
Velocity	10
Temperature	12
Species	13
Comments.....	14
Reynold Stress Turbulence Model (RSM) Simulation	16
Modifications to the original set-up	16
1-step mechanism w/o assigned inlet velocity profile	16
1-step mechanism w/ assigned inlet velocity profile	22
GriMech detailed mechanisms	29
Gri3.0 mechanism w/ assigned inlet velocity profile.....	30
Gri3.0 vs Gri2.11 mechanism	36
References	45
APPENDIX.....	46

Test case

The test case is the well-known Sandia flame D, partially premixed flame (Workshop, 2003). Averaged data of velocity components, temperature, and species' concentrations are available for validation.

Computational Domain and Mesh

We have extended the original computational domain provided in the OpenFoam Sandia flame D tutorial in the axial direction to move downstream of the location where a constant pressure condition is imposed. This was achieved by increasing the domain's extension in the "z" direction from its original value of 70 to 140. The resulting mesh now comprises 10,140 cells. Figure 1 displays an overall view of the mesh on the left, and an enlarged view of the mesh in the proximity of the pipe exit on the right.

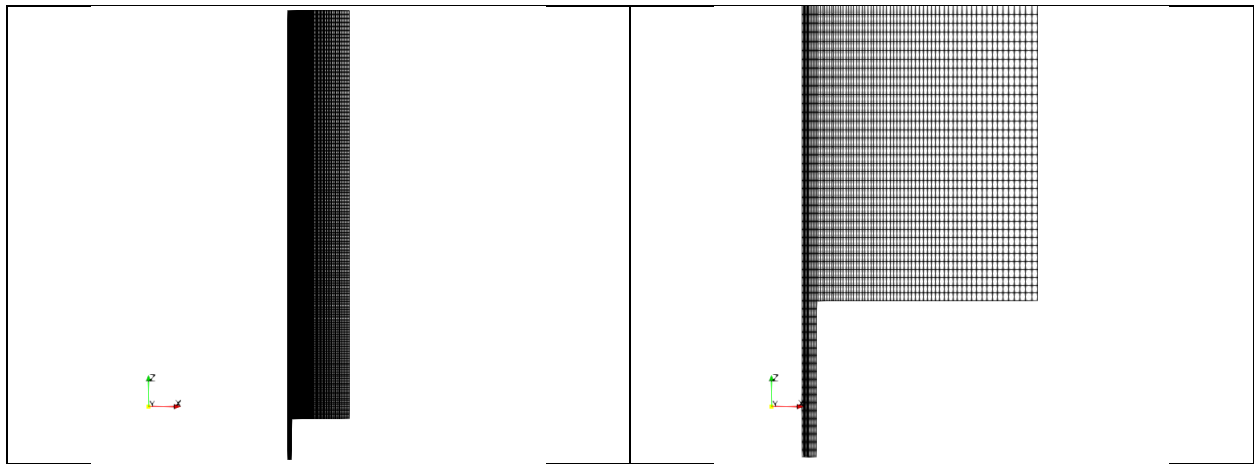


Figure 1: computational mesh

Boundary Conditions

The boundary conditions are the same as those used in the tutorial Sandia flame D provided in the openFoam distribution, and will not be discussed here.

OpenFoam settings and miscellaneous

To prevent any unintended combustion within the fuel feeding pipe, we have specified its inner portion using a dedicated entry in the topoSetDictionary. Additionally, we have implemented a function in fvOption to limit the maximum temperature within that group of cells to match the fuel's inlet temperature (294 K).

Tested reaction's mechanisms

We present here results obtained using the seven reaction's mechanisms listed in Table 1. Table 2, from (Jicang Si, 2020 (34)), and Table 3 report the parameters used to generate the corresponding CHEMKIN input files.

Table 1: tested reaction's mechanisms

Gri3.0	
1-step	
4-step Jones and Lindstedt (JL)	JL-Orig
	JL-Kim
	JL-Wang
	JL-Hu
	JL-Ann

Table 2: JL mechanisms details (Jicang Si, 2020 (34))

reaction expression		direction	$A ((\text{cm}^3/\text{mol})^n/\text{s})$	b	E_a (kcal/mol)	reaction order	refs
JL-Ori	R1	forward	7.82×10^{13}	0	30,000	$[\text{CH}_4]^{0.5}[\text{O}_2]^{1.25}$	Jones and Lindstedt ¹²
	R2	forward	3.00×10^{11}	0	30,000	$[\text{CH}_4][\text{H}_2\text{O}]$	
	R3	forward	2.75×10^{12}	0	20,000	$[\text{CO}][\text{H}_2\text{O}]$	
	R4	forward	1.21×10^{18}	-1	40,000	$[\text{H}_2]^{0.25}[\text{O}_2]^{1.5}$	
JL-Kim	R1	forward	7.82×10^{13}	0	30,000	$[\text{CH}_4]^{0.5}[\text{O}_2]^{1.25}$	Kim et al. ¹⁴
	R2	forward	3.00×10^{11}	0	30,000	$[\text{CH}_4][\text{H}_2\text{O}]$	
	R3	forward	2.75×10^{12}	0	20,000	$[\text{CO}][\text{H}_2\text{O}]$	
	R4	forward	1.30×10^{13}	0	35,000	$[\text{H}_2][\text{O}_2]^{0.5}$	
JL-Wang	R1	forward	7.82×10^{13}	0	30,000	$[\text{CH}_4]^{0.5}[\text{O}_2]^{1.25}$	Wang et al. ¹⁶
	R2	forward	3.00×10^{11}	0	30,000	$[\text{CH}_4][\text{H}_2\text{O}]$	
	R3	forward	2.75×10^{12}	0	20,000	$[\text{CO}][\text{H}_2\text{O}]$	
	R4	forward	2.50×10^{12}	0	30,000	$[\text{H}_2][\text{O}_2]^{0.5}$	
JL-Hu		reverse	3.48×10^{14}	0	95,200	$[\text{H}_2\text{O}]$	Hu et al. ¹⁷
	R1	forward	7.82×10^{13}	0	30,000	$[\text{CH}_4]^{0.5}[\text{O}_2]^{1.25}$	
	R2	forward	3.00×10^{11}	0	20,000	$[\text{CH}_4][\text{H}_2\text{O}]$	
	R3	forward	2.75×10^{12}	0	30,000	$[\text{CO}][\text{H}_2\text{O}]$	
	R4	forward	9.97×10^{12}	0	33,007	$[\text{H}_2][\text{O}_2]^{0.5}$	
JL-ANN		reverse	2.60×10^{14}	0	95,354	$[\text{H}_2\text{O}]$	present
	R1	forward	2.25×10^{11}	-0.03	21,100	$[\text{CH}_4]^{0.5}[\text{O}_2]^{1.25}$	
	R2	forward	1.14×10^{10}	-0.02	21,810	$[\text{CH}_4][\text{H}_2\text{O}]$	
	R3	forward	5.01×10^{10}	-0.03	18,000	$[\text{CO}][\text{H}_2\text{O}]$	
	R4	forward	5.23×10^{14}	-0.56	33,600	$[\text{H}_2][\text{O}_2]^{0.5}$	

Table 3: 1-step reaction mechanism parameters (Cantera User Guide, n.d.)

mechanism	direction	$A ((\text{cm}^3/\text{mol})^n/\text{s})$	b	E_a (kcal/mol)	Reaction order
1-step	forward	1.1E+10	0	20E+03	$[\text{CH}_4]^{1.0}[\text{O}_2]^{0.5}$

Results

The following sections report the computed results for the seven examined cases. Tables Table 4 through Table 8 report the comparison between the maximum values of the quantities of interest with the corresponding reference data. It is worth noting that not just the maximum Δ -quantity value matters, but also its location along the symmetry axis. This aspect is better illustrated in the x-y plots presented in the following sections.

Tables

Table 4: maximum computed temperature and percent difference with reference data ($T_{ref} = 1957$ [K])

mechanism	Max computed T [K]	% ΔT_{max} [K]
Gri3.0	2024.9	3.47
1-step	2224.9	13.69
JL-Orig	2127.6	8.72
JL-Kim	2156.8	10.21
JL-Wang	2154.1	10.07
JL-Hu	2136.5	9.17
JL-Ann	1919.7	-19.72

Table 5: maximum computed CH_4 mass fraction difference with reference data ($(CH_4)_{ref} = 0.154$ [-])

mechanism	% $(\Delta CH_4)_{max}$ [-]
Gri3.0	1.37
1-step	1.69
JL-Orig	1.75
JL-Kim	1.36
JL-Wang	1.69
JL-Hu	1.23
JL-Ann	1.36

Table 6: maximum computed CO_2 mass fraction difference with reference data ($(CO_2)_{ref} = 0.11$ [-])

mechanism	% $(\Delta CO_2)_{max}$ [-]
Gri3.0	11.64
1-step	40.36
JL-Orig	28.73
JL-Kim	21.00
JL-Wang	20.45
JL-Hu	18.55
JL-Ann	-67.27

Table 7: maximum computed H_2O mass fraction difference with reference data ($(H_2O)_{ref} = 0.117$ [-])

mechanism	$\%(\Delta H_2O)_{max}$ [-]
Gri3.0	7.44
1-step	8.29
JL-Orig	11.37
JL-Kim	11.88
JL-Wang	14.62
JL-Hu	9.23
JL-Ann	-15.38

Table 8: maximum computed CO mass fraction difference with reference data ($(CO)_{ref} = 0.048$ [-])

mechanism	$\%(\Delta CO)_{max}$ [-]
Gri3.0	27.08
1-step	-
JL-Orig	180.63
JL-Kim	22.92
JL-Wang	25.00
JL-Hu	45.21
JL-Ann	45.00

Table 9: CPU time for 50000 iterations (1500 w/o reaction + 48500 w/ reaction) on 1 Intel i7-975H CPU @ 2.60GHz

Reaction mechanism	CPU time [s]
gri3.0	20923
1-step	5258
4-step-JL-Orig	7632
4-step-JL-Kim	7249
4-step-JL-Wang	6850
4-step-JL-Hu	6912
4-step-JL-Ann	6992

Table 10: overall error and computational cost

mechanism	overall error	Norm. overall error	Normalized computational cost
Gri3.0	10.20	1	3.98
1-step	16.00	1.57	1
JL-Orig	46.24	4.53	1.45
JL-Kim	13.47	1.32	1.38
JL-Wang	14.37	1.40	1.30
JL-Hu	16.68	1.64	1.31

Convergence

Figure 2 shows the numerical residuals for the seven examined cases. Exam of Figure 2 suggests the unsteady nature of the phenomenon under study.

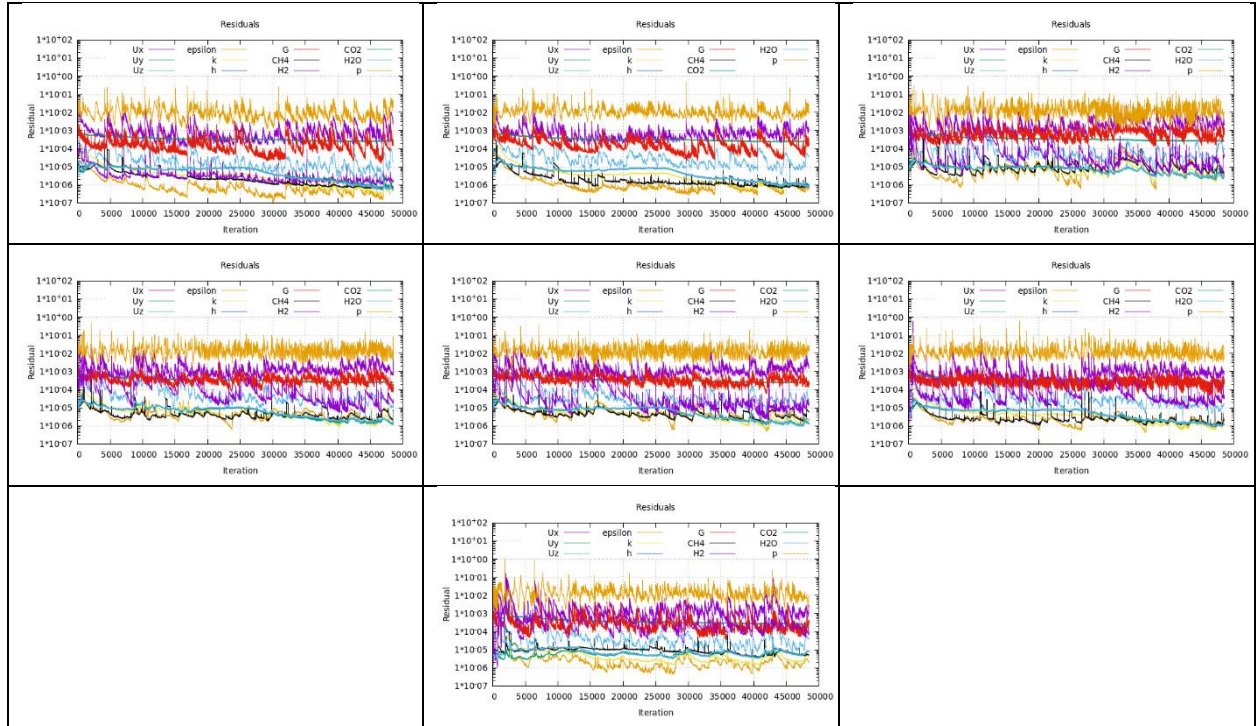


Figure 2: residuals' convergence history: top: gri3.0 (left), 1-step (center), 4-step-JL-Orig (right); middle: 4-step-JL-Kim (left), 4-step-JL-Wang (center), 4-step-JL-Hu (right); bottom: 4-step-JL-Ann (center)

Color fields

Fields of temperature and combustion source term are presented here.

Temperature

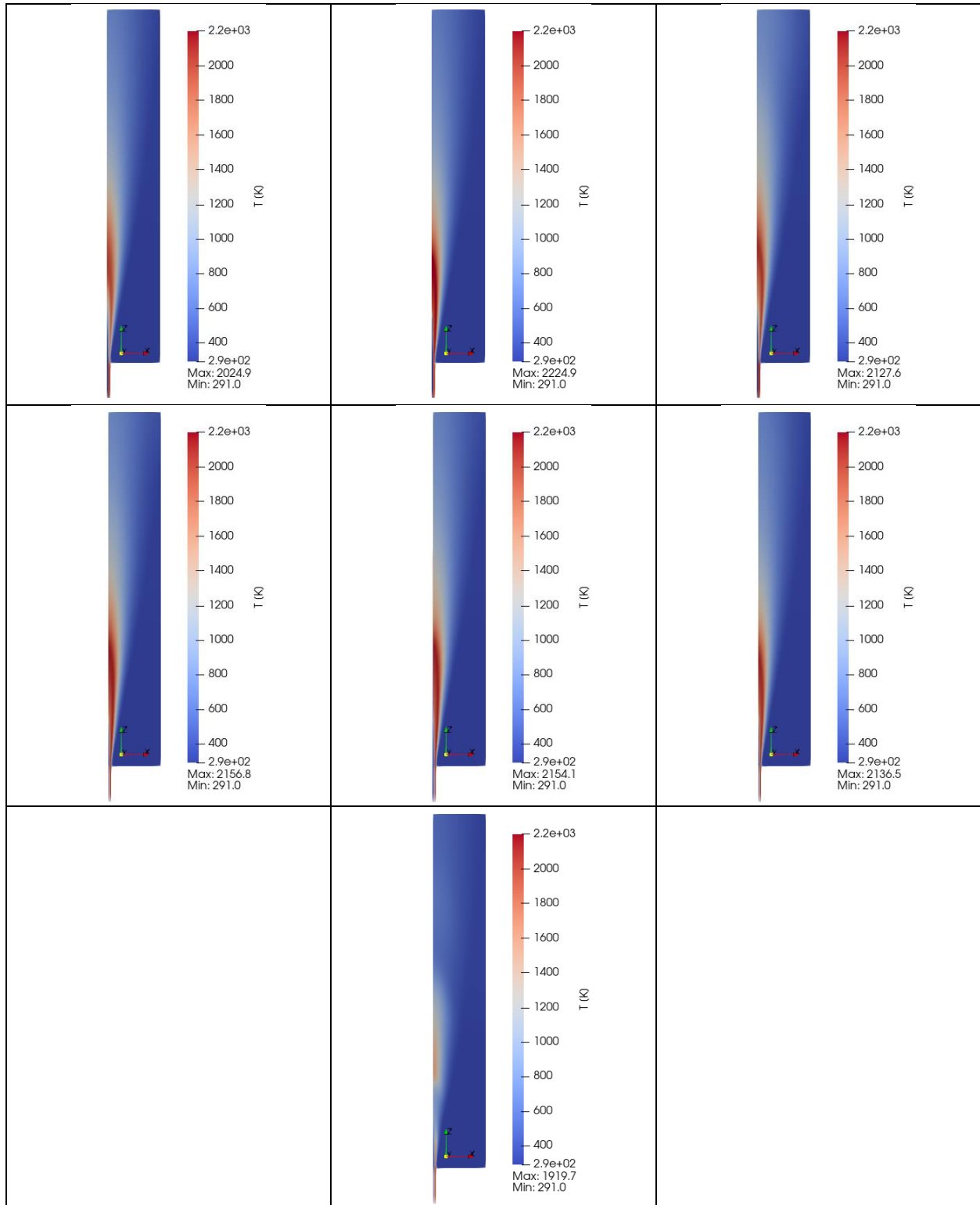


Figure 3: temperature color map: top: gri3.0 (left), 1-step (center), 4-step-JL-Orig (right); middle: 4-step-JL-Kim (left), 4-step-JL-Wang (center), 4-step-JL-Hu (right); bottom: 4-step-JL-Ann (center)

Flame front

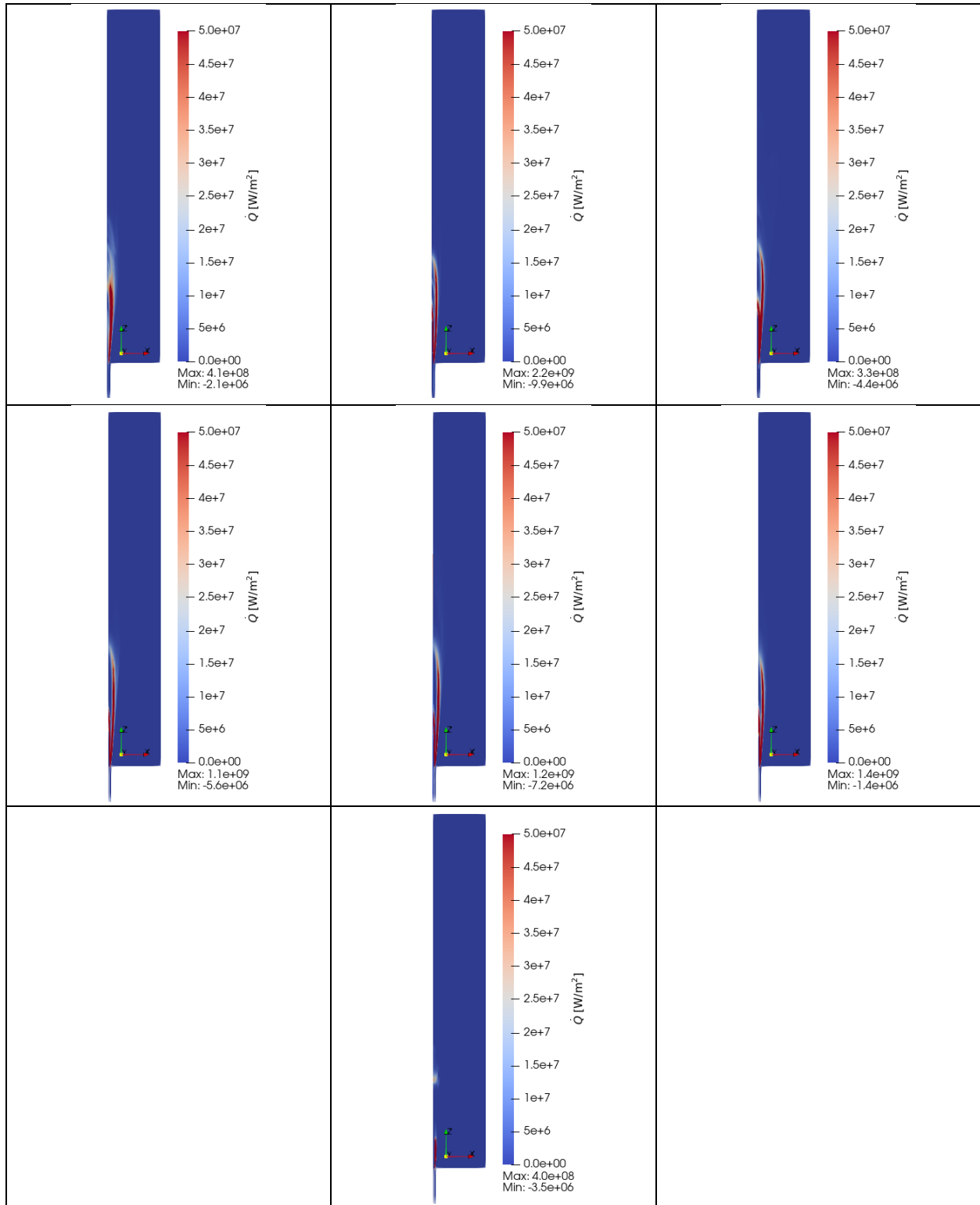


Figure 4: flame front position, identified by \dot{Q} : top: gri3.0 (left), 1-step (center), 4-step-JL-Orig (right); middle: 4-step-JL-Kim (left), 4-step-JL-Wang (center), 4-step-JL-Hu (right); bottom: 4-step-JL-Ann (center)

XY-plots

Figures from Figure 5 through Figure 9 show axial plots of velocity components, temperature and chemical species.

Velocity

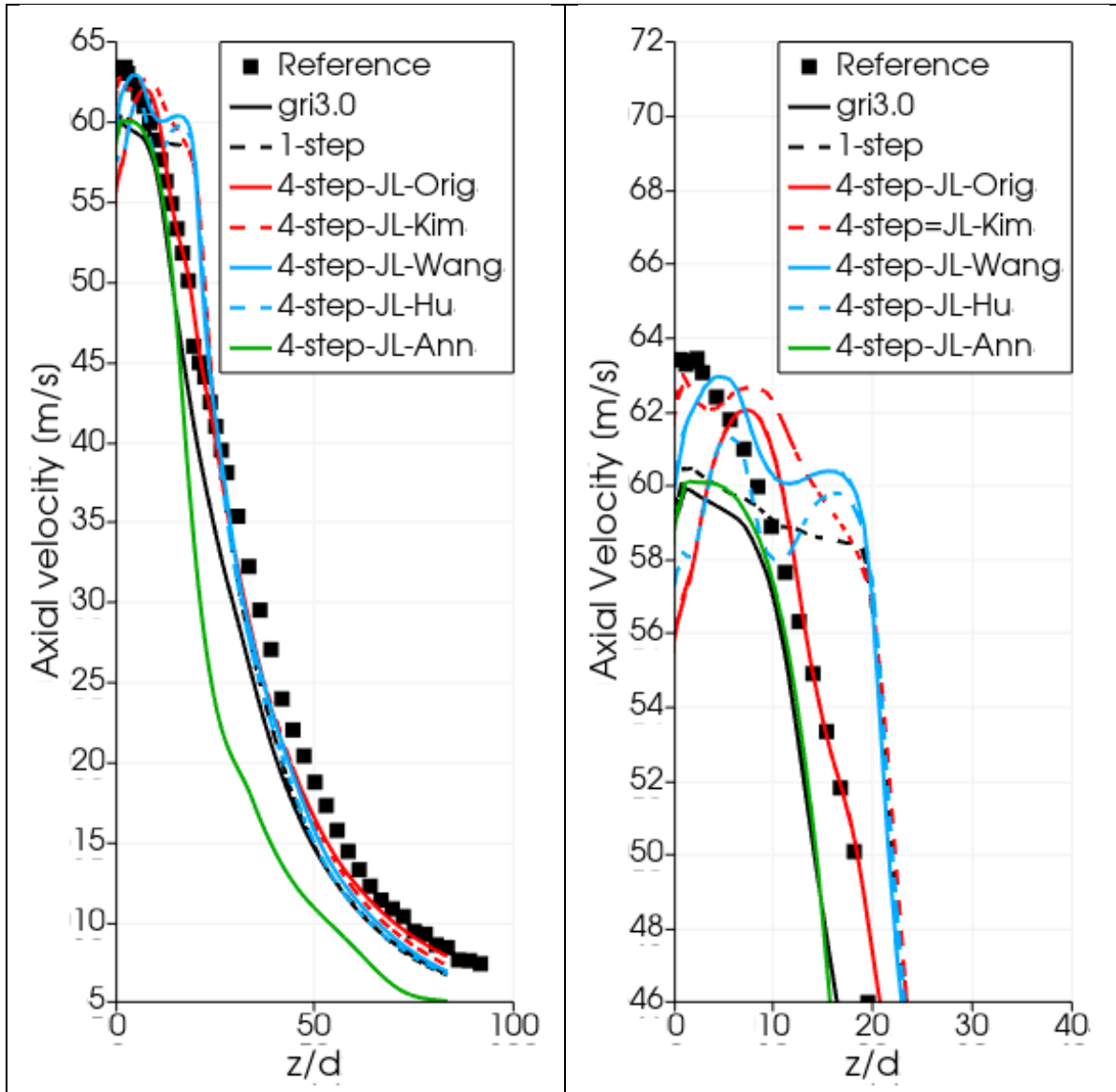


Figure 5: axial velocity component along the symmetry axis (left) and a magnified detail around its maximum value (right)

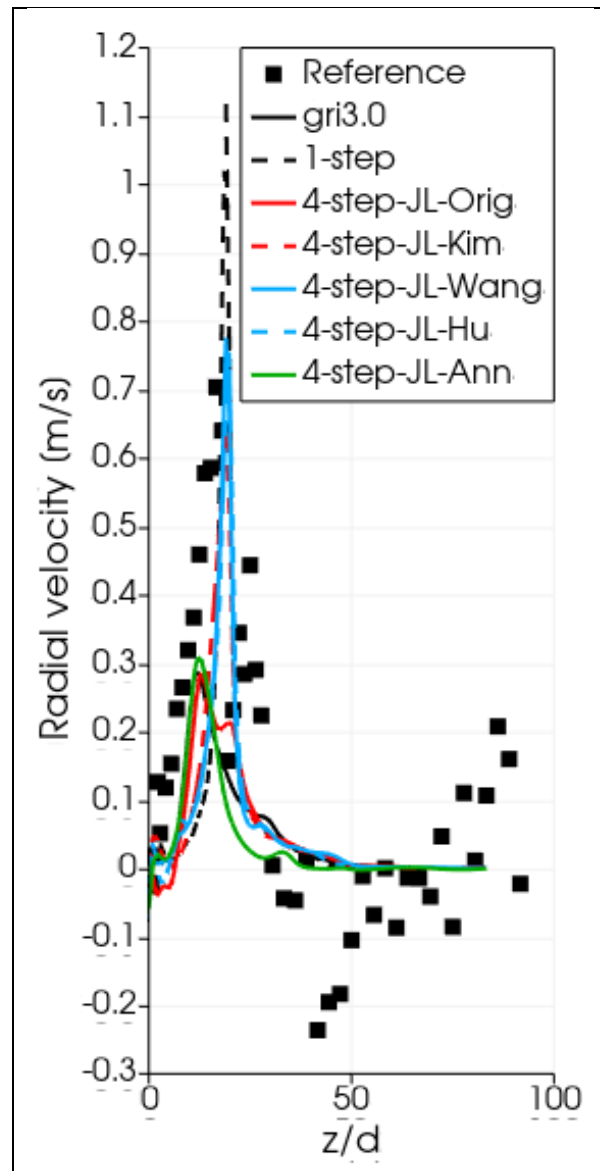


Figure 6: radial velocity component along the symmetry axis

Temperature

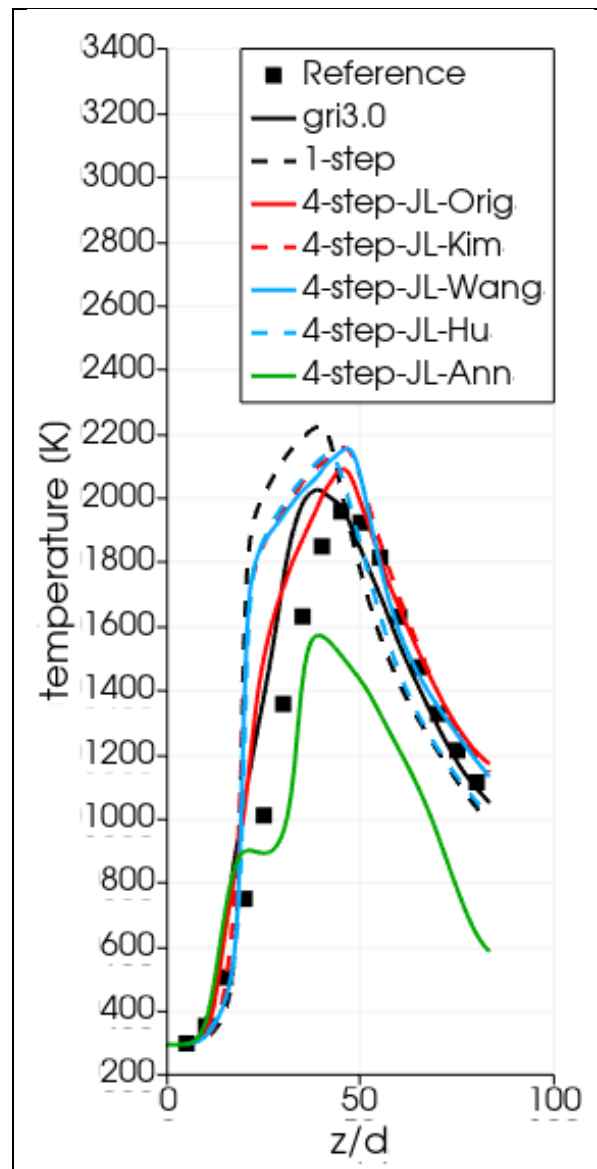


Figure 7: temperature along the symmetry axis

Species

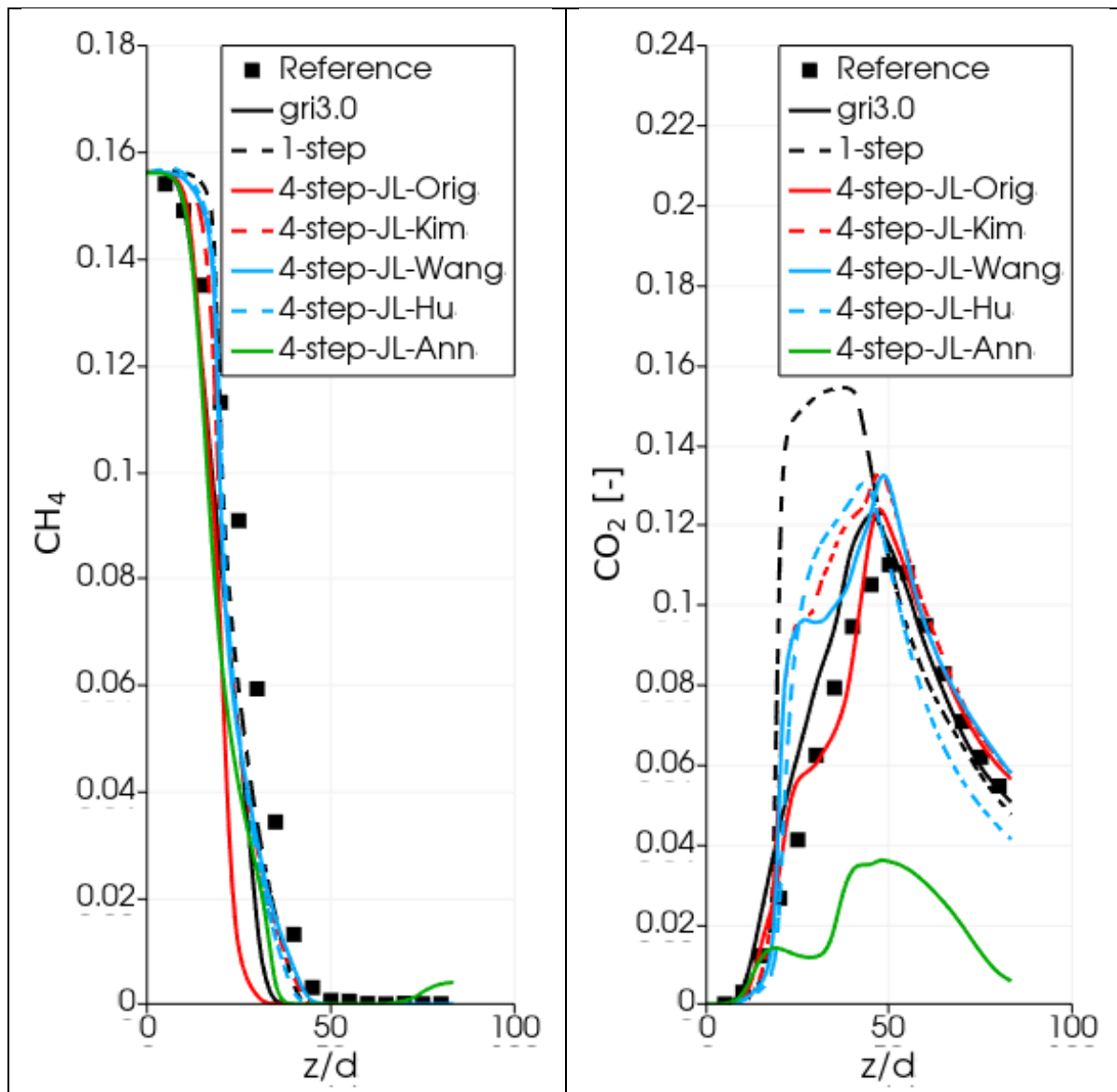


Figure 8: plots of CH_4 (left) and CO_2 (right) mass fraction along the symmetry axis

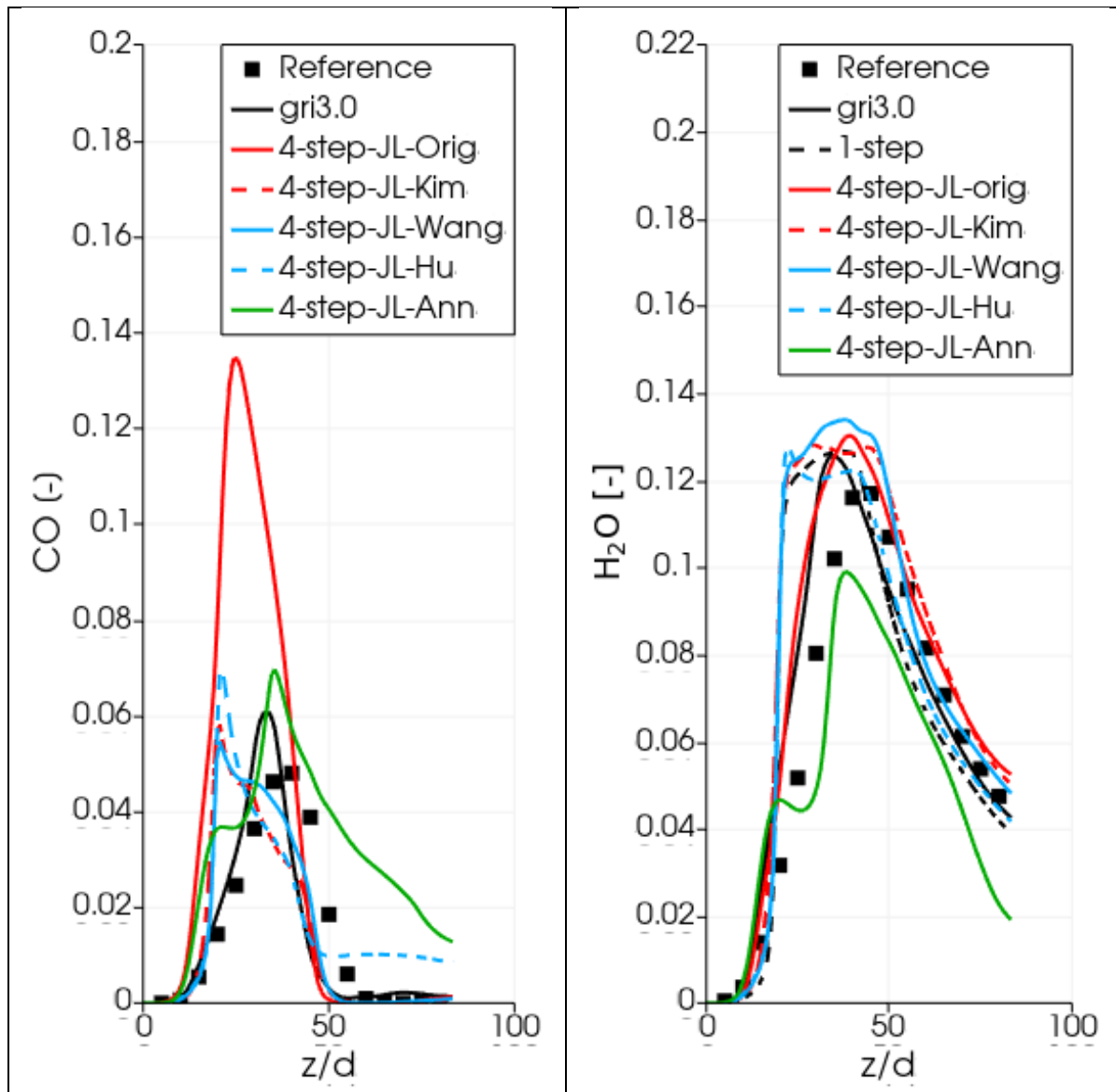


Figure 9: plots of CO (left) and H₂O (right) mass fraction along the symmetry axis

Comments

As a general comment, the accuracy of computed results, both qualitative and quantitative, strongly depends on the reaction mechanism used. Even for the same reaction mechanism (JL), the quantities' maximum values and location along the flame's axis can vary greatly.

Figure 2 demonstrates the flow unsteadiness, which is further illustrated in Figure 5, showing the wavy behavior of the axial velocity component along the axis.

Figure 5 indicates that all simulations underestimate the correct maximum axial velocity value, possibly due to the use of uniform velocity and turbulence values at the inlet instead of velocity and turbulence profiles, which are recommended as inlet boundary conditions (Workshop, 2003).

In Figure 6, only the JL-Wang, JL-Kim, and JL-Hu mechanisms predict the correct radial velocity peak value. The 1-step reaction overestimates the peak value, whereas the remaining ones do not provide any meaningful prediction. Moreover, none of the tested mechanisms captures the correct wavy form of the velocity field further downstream the axis, as indicated by the negative peak at around $z/d = 40$ and the successive positive one at around $z/d = 80$. Downstream of the first positive peak, all solutions show a flat radial velocity pattern.

Table 4 reports the difference (in percent) between the maximum predicted temperature value along the axis and the reference value, and Figure 7 shows the temperature distribution along the axis. As expected, the gri3.0 mechanism best estimates the maximum temperature (% error = 3.5 circa), while the 1-step reaction gives the worst prediction (% error = 13.7 circa). All other 4-step mechanisms provide similar error levels (9-10% circa), except for the JL-Ann, which is totally off. Figure 3 and Figure 4 give reason of the non-correct prediction provided by the JL-Ann mechanism, as the flame's blow-off is evident. In We will not further discuss results obtained with the JL-Ann mechanism. Examining Figure 7 shows that only the JL-Orig mechanism almost correctly predicts the position of the maximum location of the temperature curve. All other curves have their maximum either to the left or right of the reference data.

It's important to remember that the width of a flame's brush is not solely determined by the reaction mechanism but is also influenced by the characteristics of the overall flow, which are governed by turbulence or the interplay between turbulence and chemistry. Although the present study employs the same turbulence model (standard κ - ϵ) for all simulated cases, there's no assurance at this stage that using a different turbulence model wouldn't lead to a significantly different behavior of the chemical mechanisms being tested.

Table 6 (CO_2) shows again that the best prediction is given by gri3.0 and that the error is maximum in the case of the 1-step mechanism. All 4-step mechanisms, with the exception of the JL-Orig (29% circa) give a similar error level (20% circa).

Table 8 (CO) shows a somewhat unexpected finding. All tested mechanisms greatly over-estimate the production of CO, including the gri3.0. With the exception of the JL-Orig mechanism, which is totally off (this behavior is also reported in Jicang Si, 2020 (34)), and of the JL-Hu, predictions given by the other 4-step mechanisms are in the same range of that provided by the more sophisticated gri3.0.

Finally, Table 7 (H_2O), shows once again that the lowest error is found for the gri3.0 mechanism (7% circa), followed by the 1-step (8% circa). All 4-step mechanisms provided an error varying from 9% to 15% circa.

We can estimate the overall accuracy of the tested reaction mechanism by summing up the maximum percent error from Table 4 to Table 8. However, it is important to note that this exercise only provides partial information about the accuracy of the tested mechanisms, as it does not take into account the predicted shape of the flame. The overall error, computed in this way, is presented in Table 10. The summation is divided by five for gri3.0 and all 4-step mechanisms, and by four for the 1-step mechanism, to account for the fact that the 1-step reaction cannot predict CO production. The second column of Table 10 shows the normalized overall error with respect to the best mechanism, gri3.0. The third column summarizes the normalized computational cost of each mechanism, relative to the least expensive one (the 1-step mechanism), as shown in Table 9.

Reynold Stress Turbulence Model (RSM) Simulation

We took a preliminary step towards reworking the 1-step combustion mechanism simulation by replacing the original κ - ϵ model with an RSM turbulence model. Our aim was twofold: firstly, to gain familiarity with the use of the RSM model, and secondly, to explore the potential impact of turbulence modeling on the simulation results.

Modifications to the original set-up

We modified some of the original 1-step simulation files to ensure the simulation ran smoothly without encountering numerical divergence. Specifically, we took the following steps:

- We created two different versions of the fvSolution file to adjust solution parameters during the non-reactive and reactive phases of the simulation. The Allrun script handles these files at runtime by copying one or the other into the required fvSolution file. The two files are named fvSolution.cold and fvSolution.hot, with obvious significance in their names.
- In the fvSolution.cold file, we introduced the following modifications:
 - Changed rDeltaTSmoothingCoeff from 0.025 to 0.25
 - Set the fields relaxation factor to 0.8 from the original 1.0
 - Set a relaxation factor of 0.3 for the equation for epsilon.
- In the fvSolution.hot file, we set the relaxation factors for all fields and equations to 0.5.
- We set the turbulence model in the turbulenceProperties file to LRR (Launder, Reece, and Rodi).
- We created a file named R that contains boundary conditions for the Reynolds stresses tensor R. This file is available in the appendix.

1-step mechanism w/o assigned inlet velocity profile

The following figures offer a comparison of the numerical residual convergence histories and computed results between the standard κ - ϵ and RSM models.

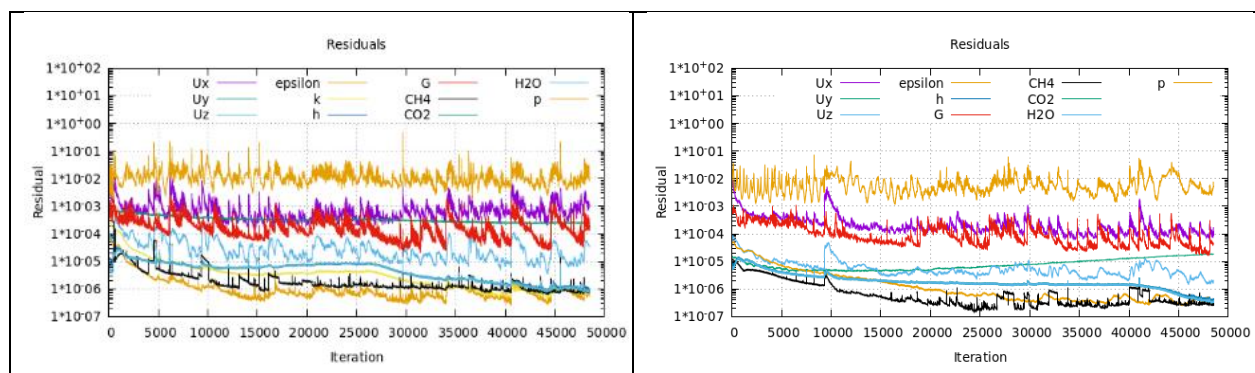


Figure 10: residual convergence history, standard κ - ϵ model (left), RSM (right)

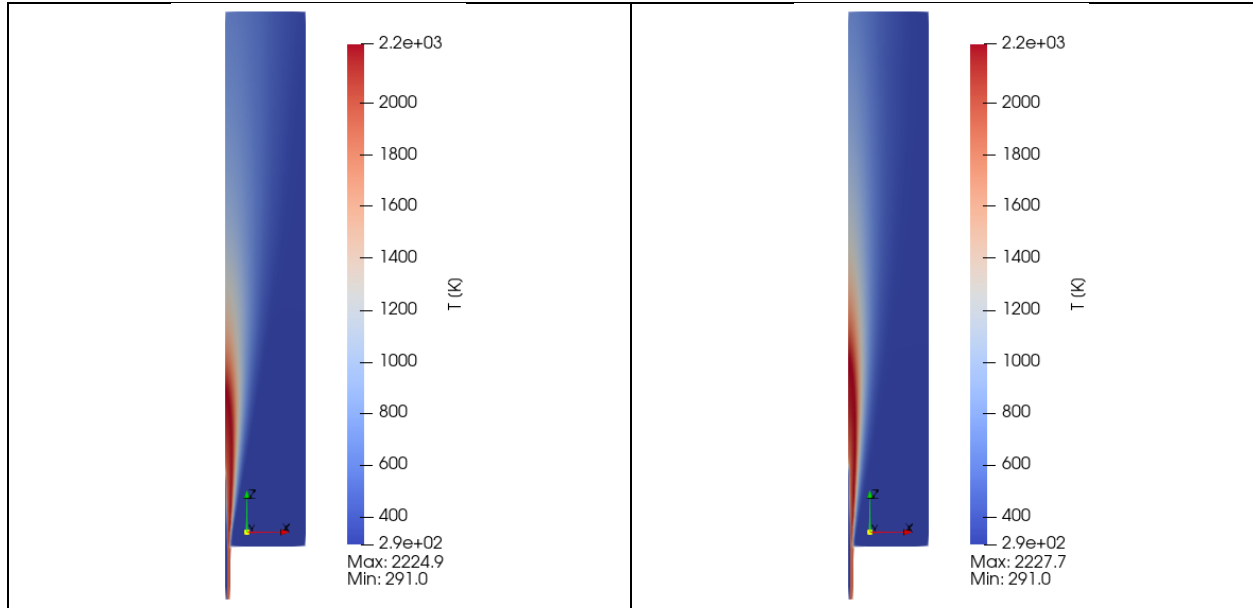


Figure 11: temperature field, standard $k-\epsilon$ model (left), RSM (right)

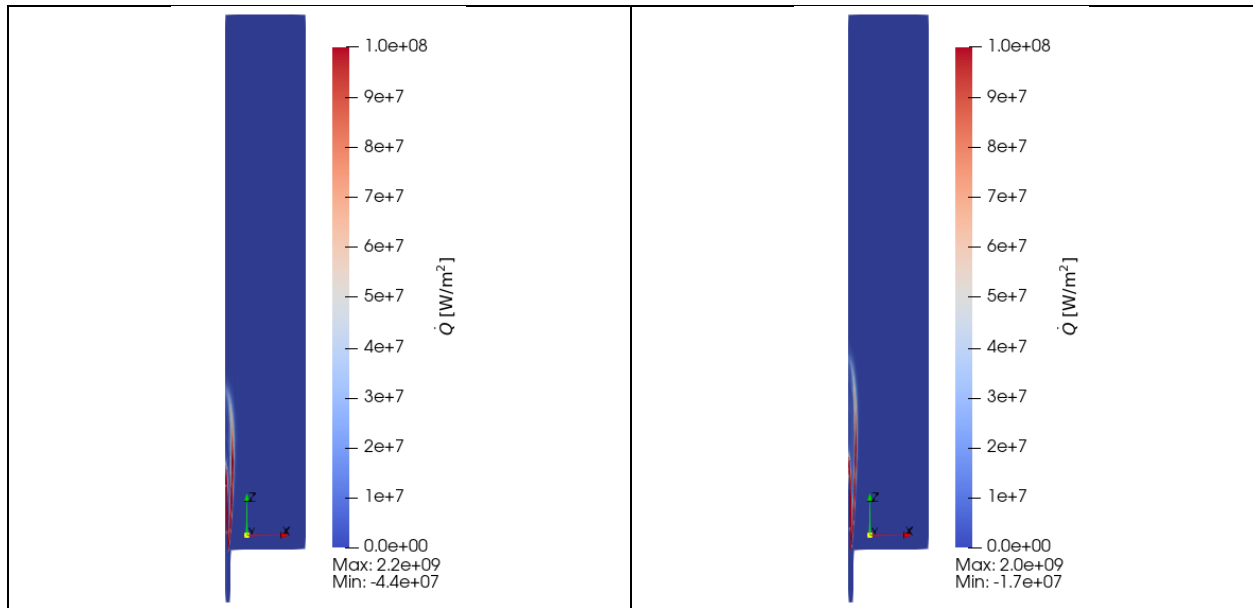


Figure 12: flame front position, identified by \dot{Q} : standard $k-\epsilon$ model (left), RSM (right), the RSM model predicts a longer flame than the standard $k-\epsilon$ model does

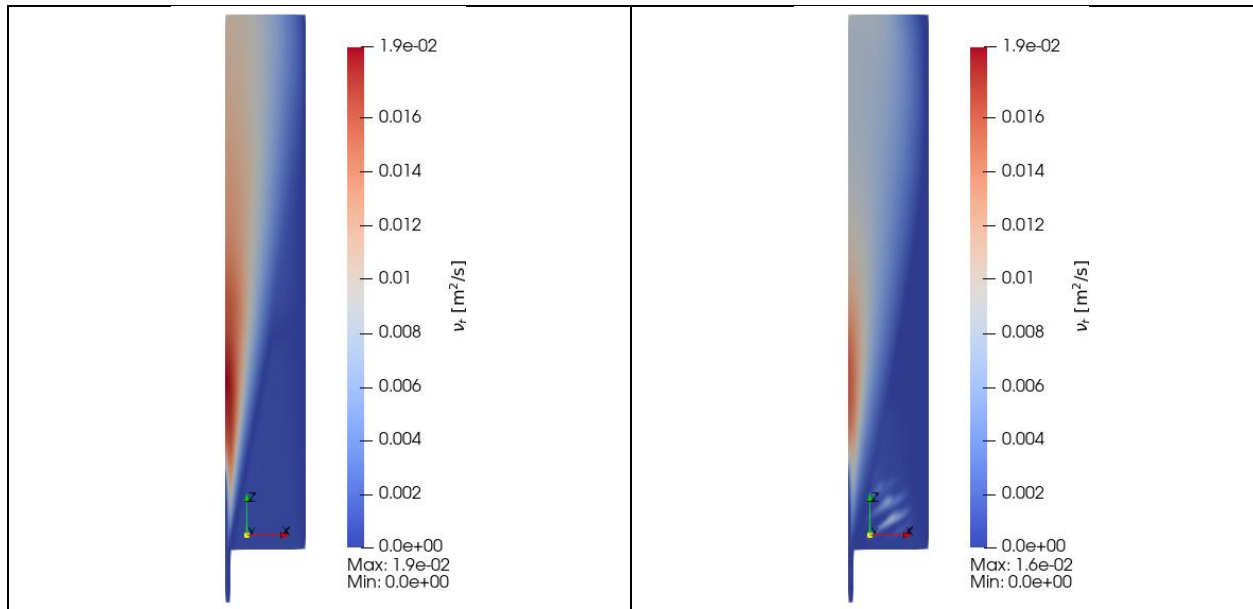


Figure 13: kinematic turbulent viscosity: standard κ - ϵ model (left), RSM (right), the RSM model predicts a generally lower turbulence level than the standard κ - ϵ model does; moreover, some disturbances are visible in the RSM solution in the proximity of the air inlet

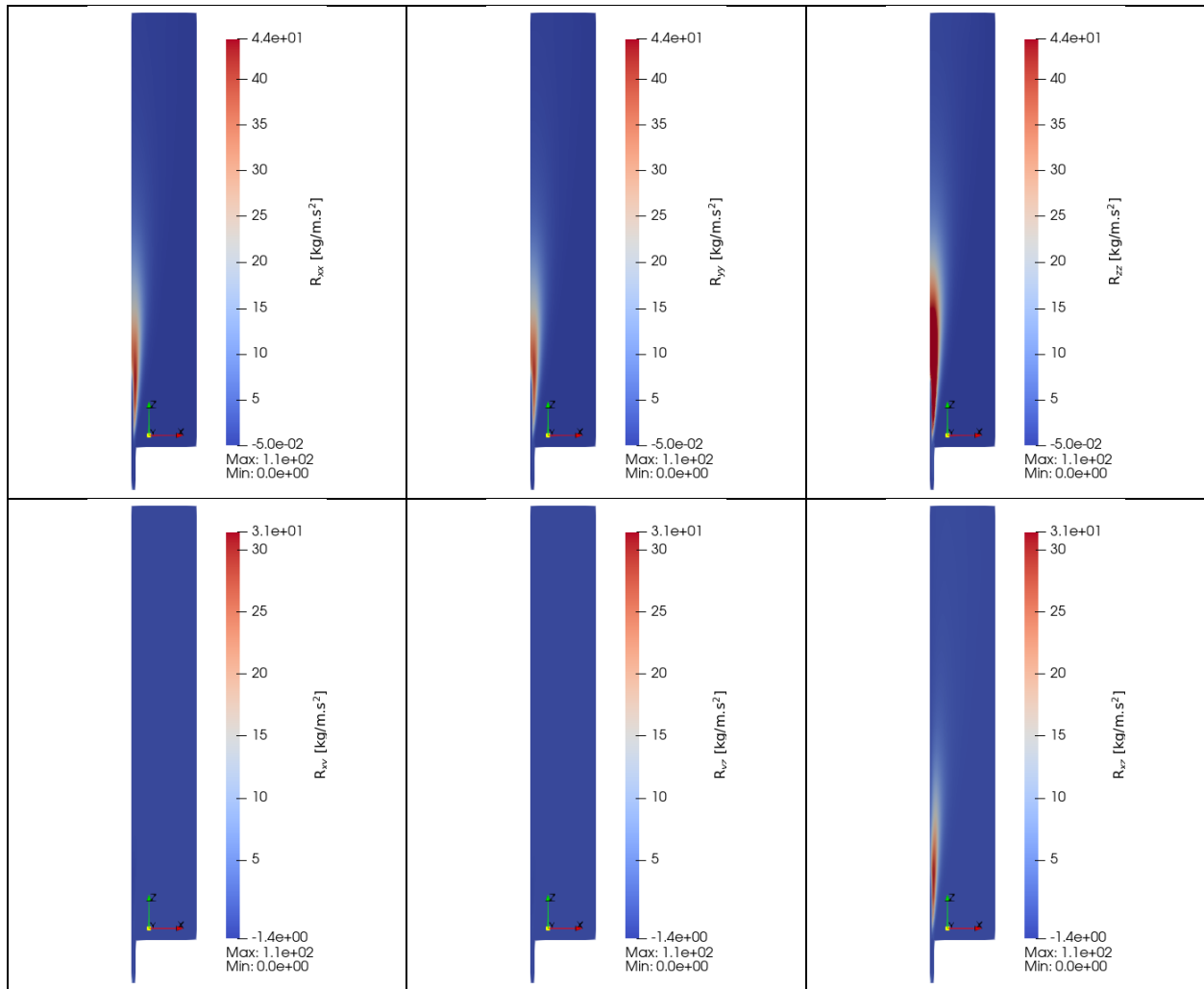


Figure 14: 1-step w/o inlet velocity profile, Reynold stress components: top: R_{xx} (left), R_{yy} (center), R_{zz} (right); bottom: R_{xy} (left), R_{yz} (center), R_{zx} (right)

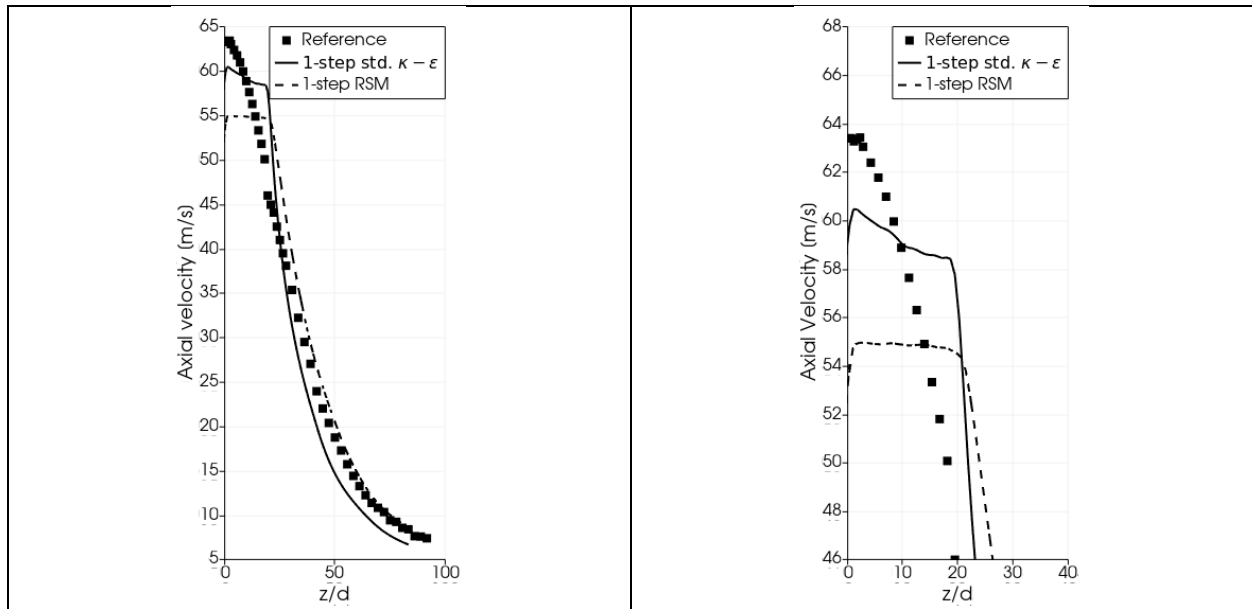


Figure 15: axial velocity component along the symmetry axis (left) and a magnified detail around its maximum value (right)

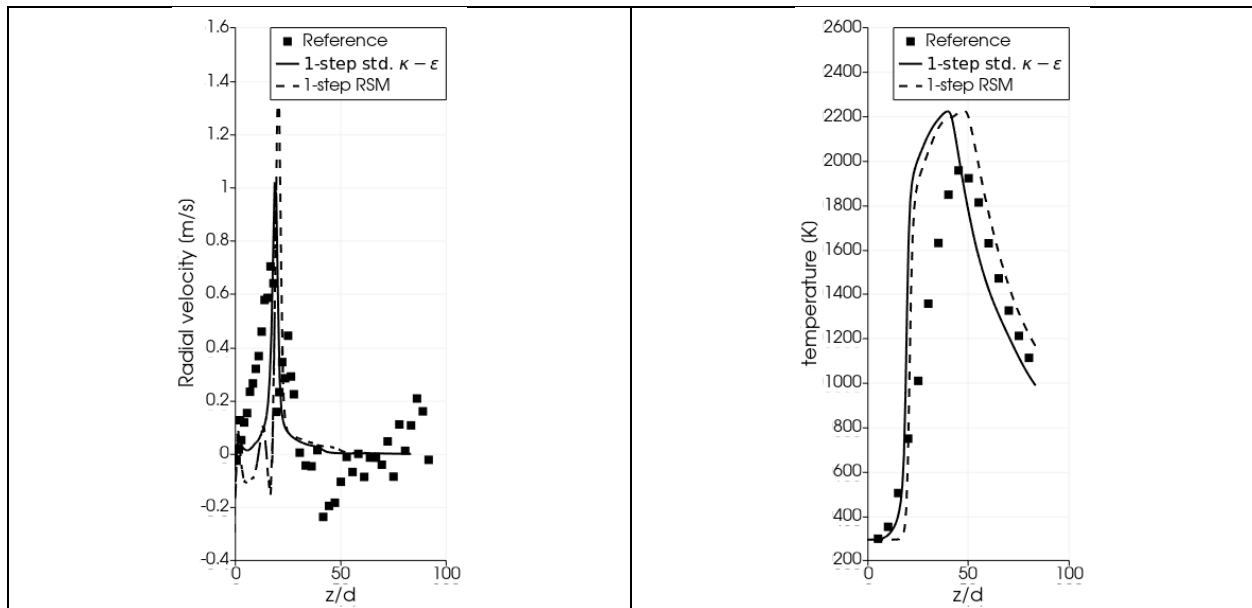


Figure 16: radial velocity component (left) and temperature (right) along the symmetry axis

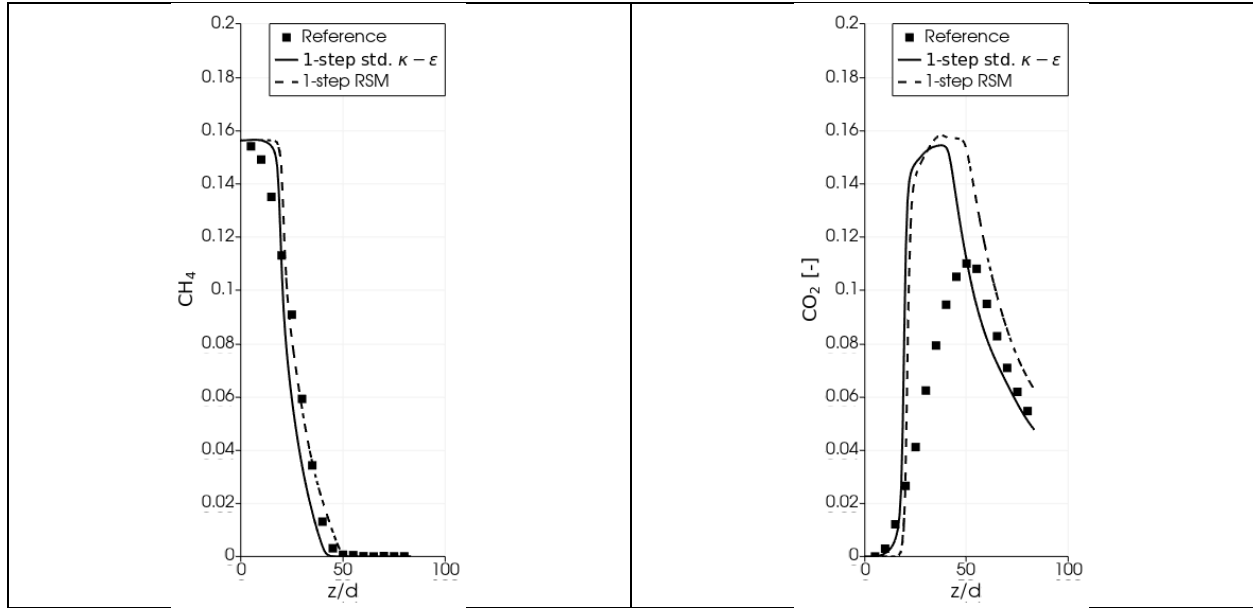


Figure 17: plots of CH_4 (left) and CO_2 (right) mass fraction along the symmetry axis

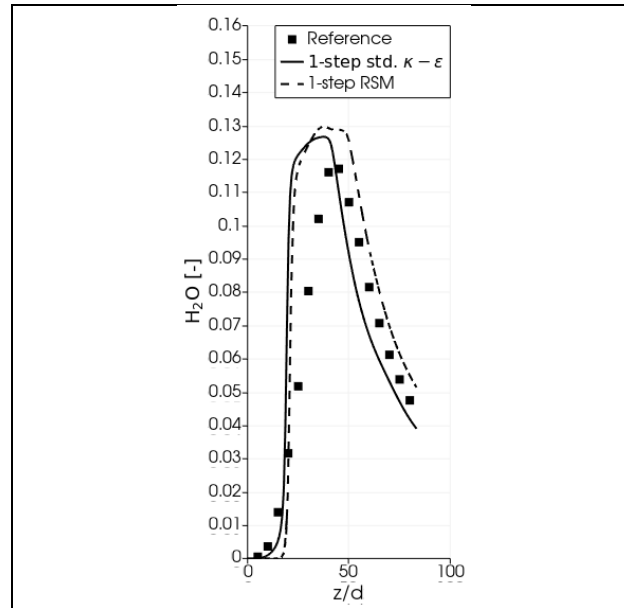


Figure 18: plots of H_2O mass fraction along the symmetry axis

1-step mechanism w/ assigned inlet velocity profile

This section reports results obtained with the prescribed inlet velocity profile given in (Workshop, 2003). The following figures offer a comparison of the numerical residual convergence histories and computed results between the standard κ - ϵ and RSM models.

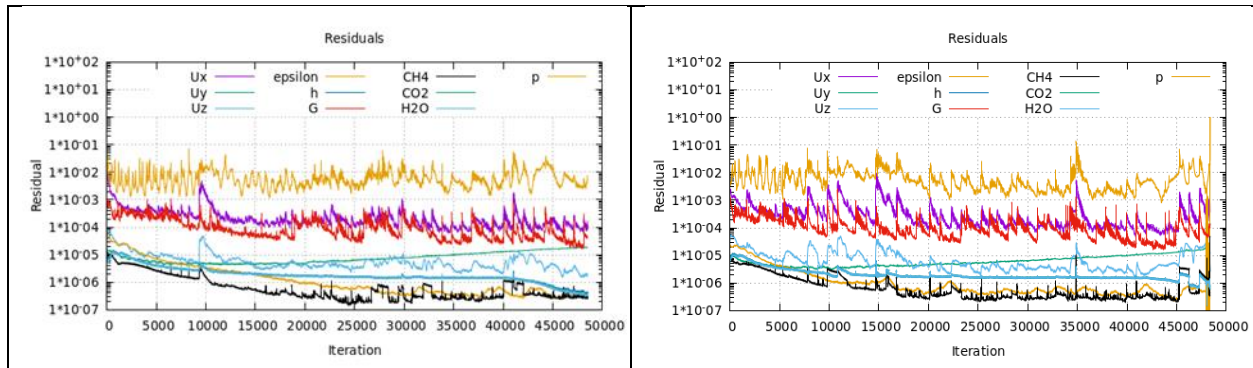


Figure 19: residual convergence history, RSM w/o inlet velocity profile (left), RSM w/ inlet velocity profile (right)

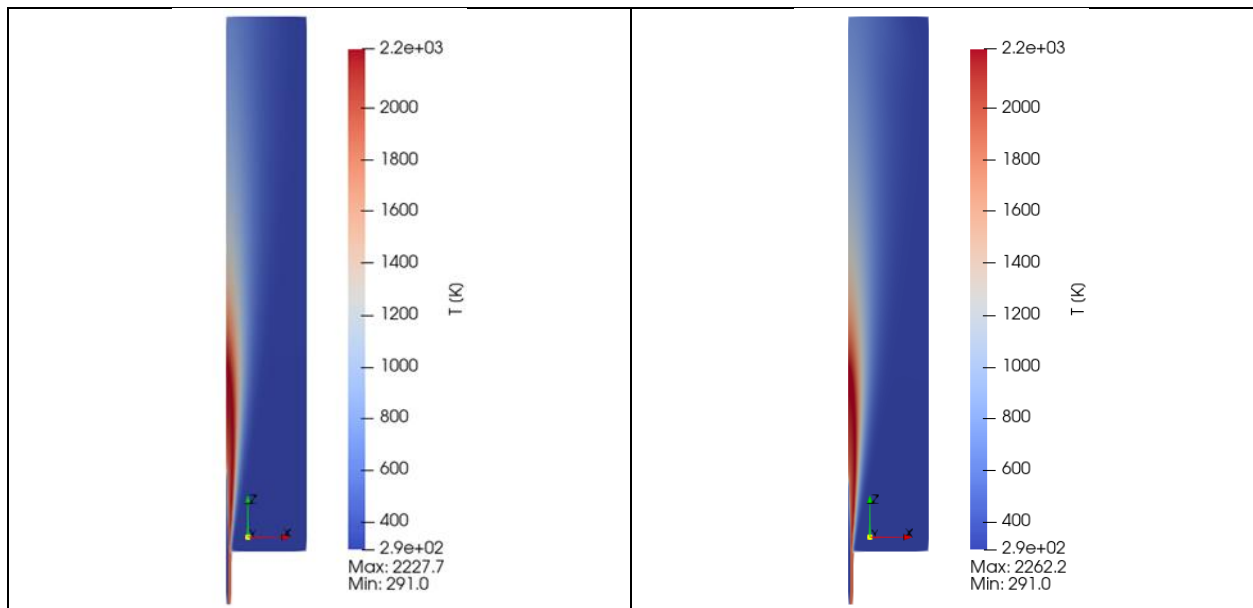


Figure 20: temperature field, RSM w/o inlet velocity profile (left), RSM w/ inlet velocity profile (right)

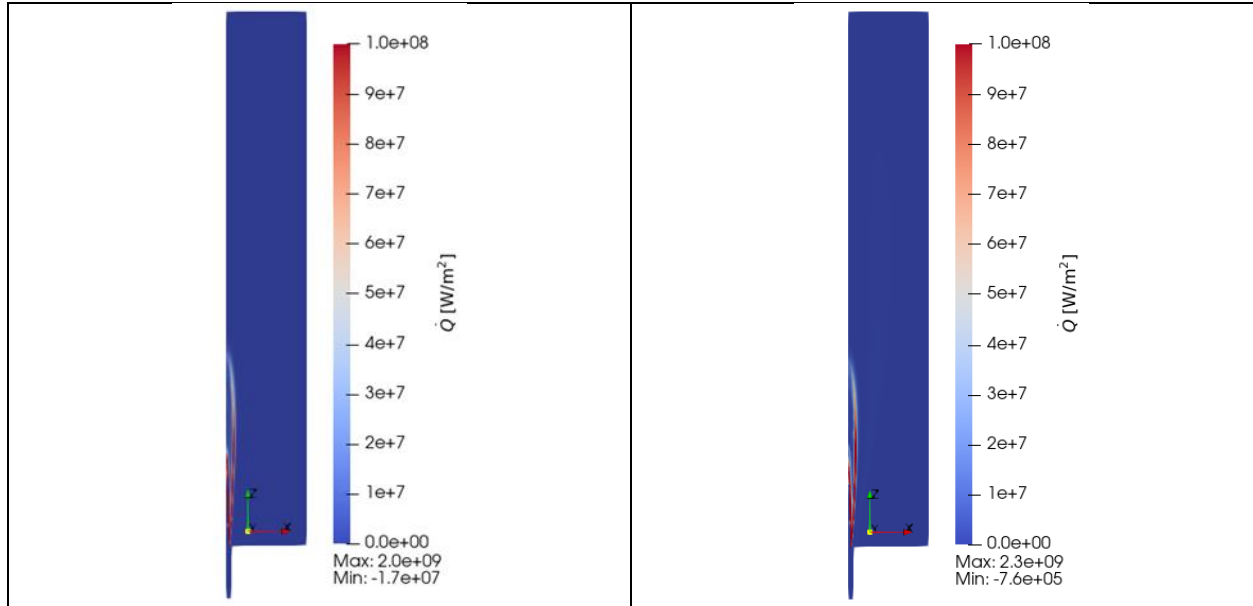


Figure 21: flame front position, identified by \dot{Q} RSM w/o inlet velocity profile (left), RSM w/ inlet velocity profile (right)

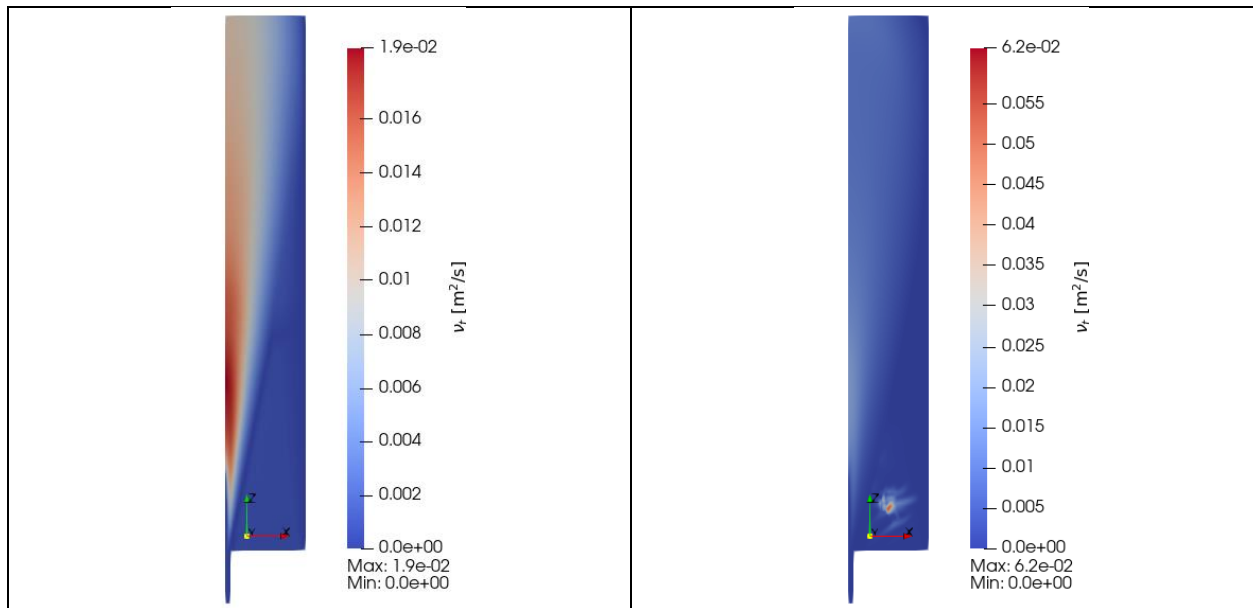


Figure 22: kinematic turbulent viscosity: RSM w/o inlet velocity profile (left), RSM w/ inlet velocity profile (right)

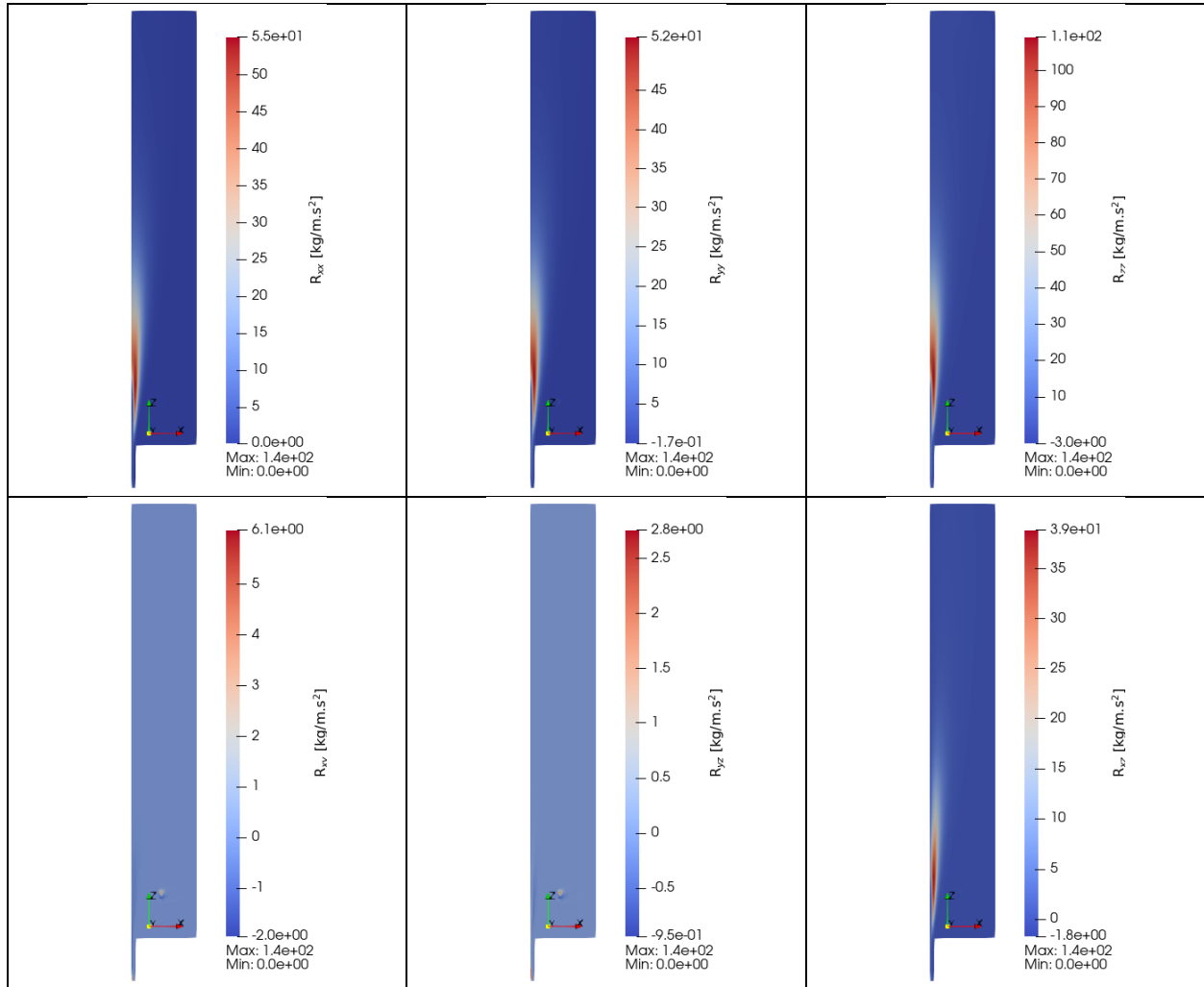


Figure 23: 1-step w/ inlet velocity profile, Reynold stress components: top: R_{xx} (left), R_{yy} (center), R_{zz} (right); bottom: R_{xy} (left), R_{yz} (center), R_{zx} (right)

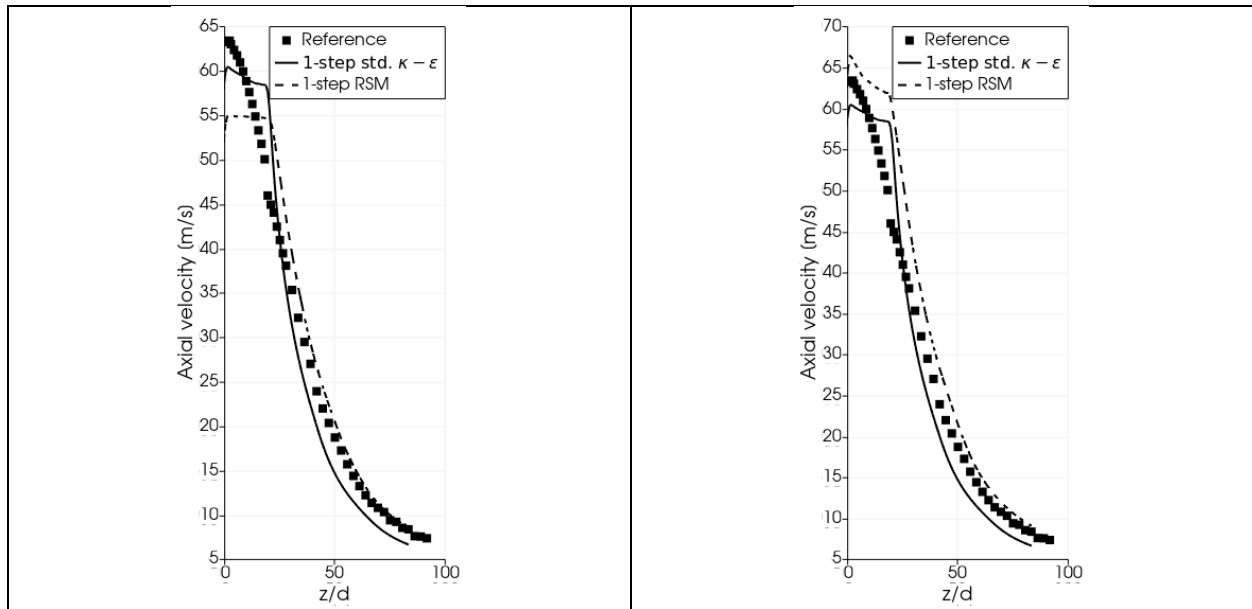


Figure 24: axial velocity component along the symmetry axis: RSM w/o inlet velocity profile (left), RSM w/ inlet velocity profile (right)

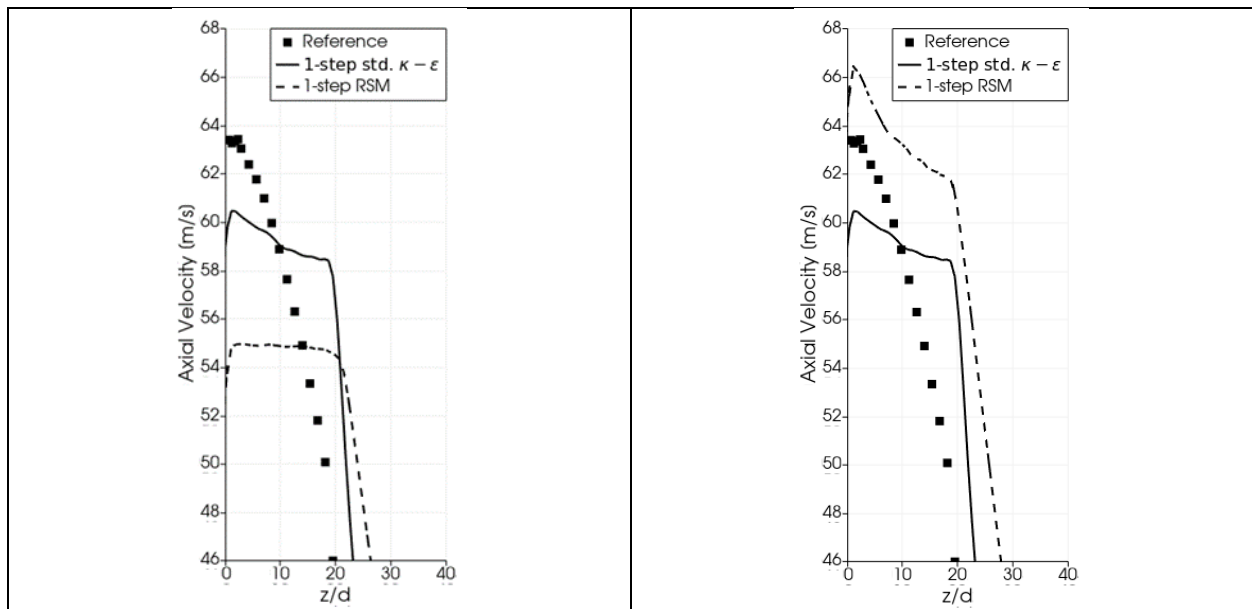


Figure 25: magnified detail around the axial velocity maximum value: RSM w/o inlet velocity profile (left), RSM w/ inlet velocity profile (right)

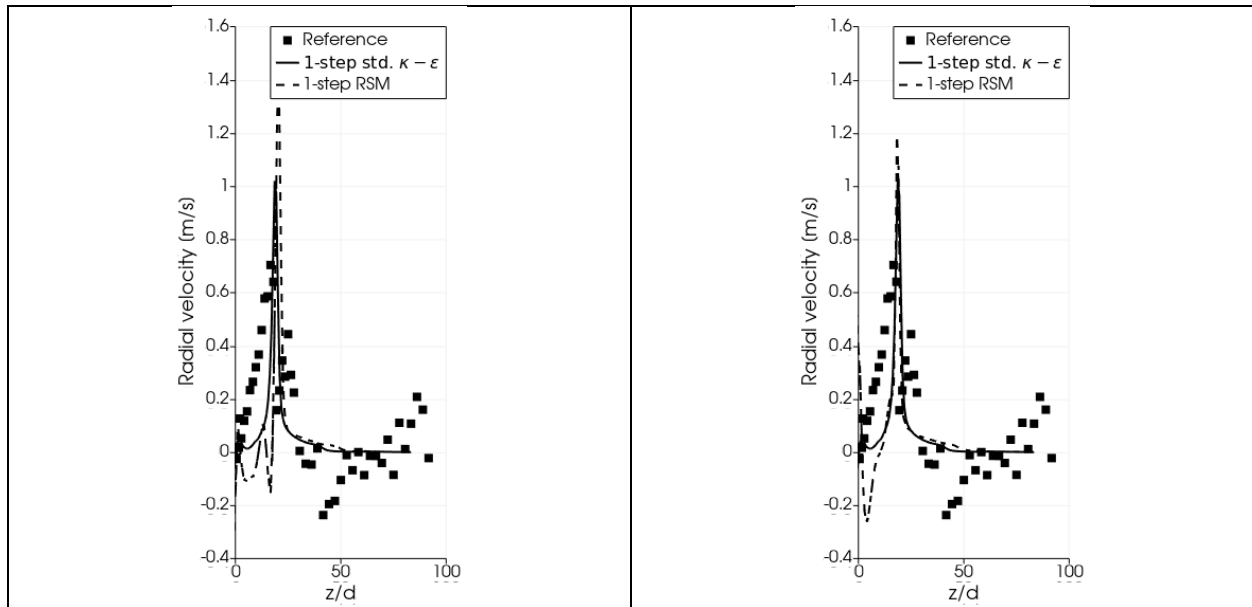


Figure 26: radial velocity component along the symmetry axis: RSM w/o inlet velocity profile (left), RSM w/ inlet velocity profile (right)

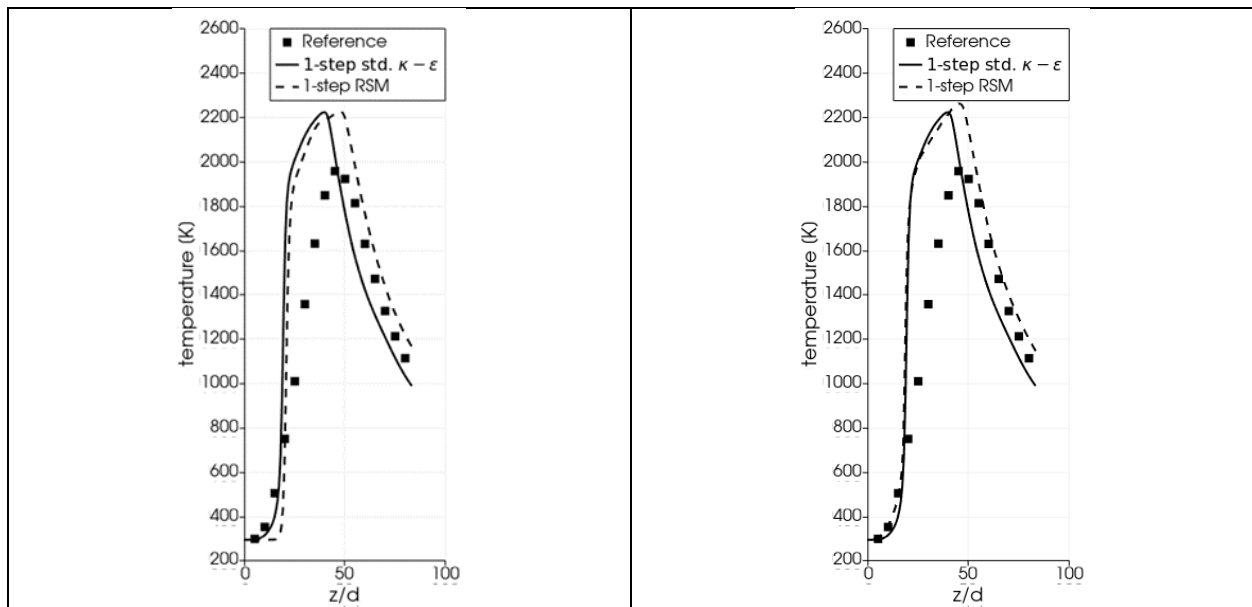


Figure 27: temperature along the symmetry axis: RSM w/o inlet velocity profile (left), RSM w/ inlet velocity profile (right)

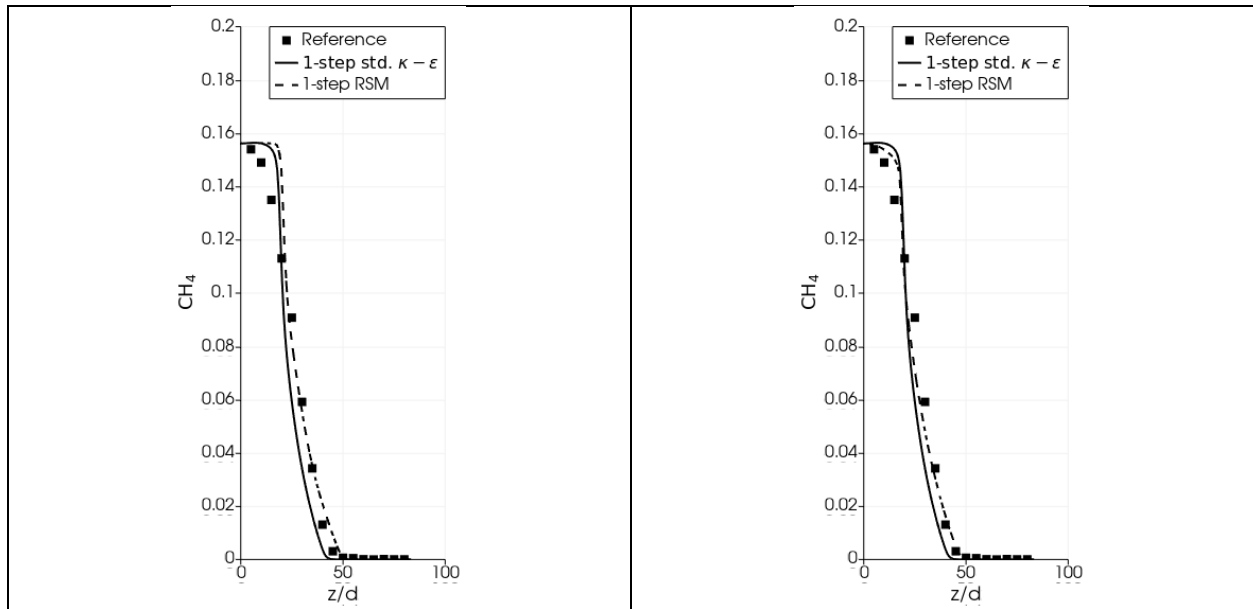


Figure 28: plots of CH_4 mass fraction along the symmetry axis: RSM w/o inlet velocity profile (left), RSM w/ inlet velocity profile (right)

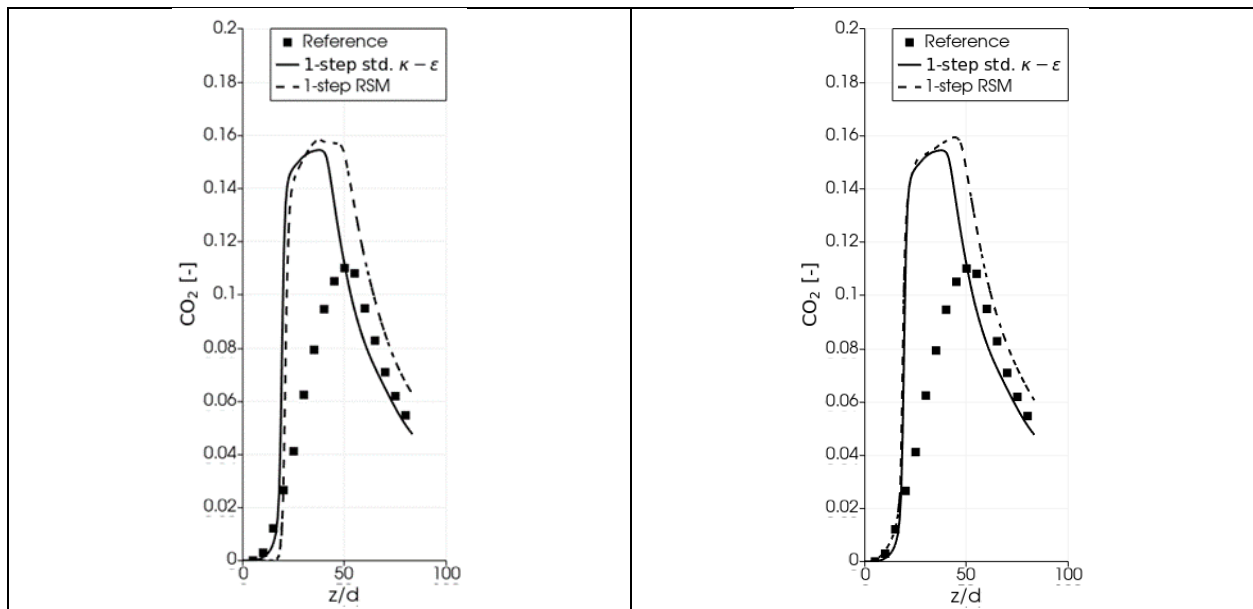


Figure 29: plots of CO_2 mass fraction along the symmetry axis: RSM w/o inlet velocity profile (left), RSM w/ inlet velocity profile (right)

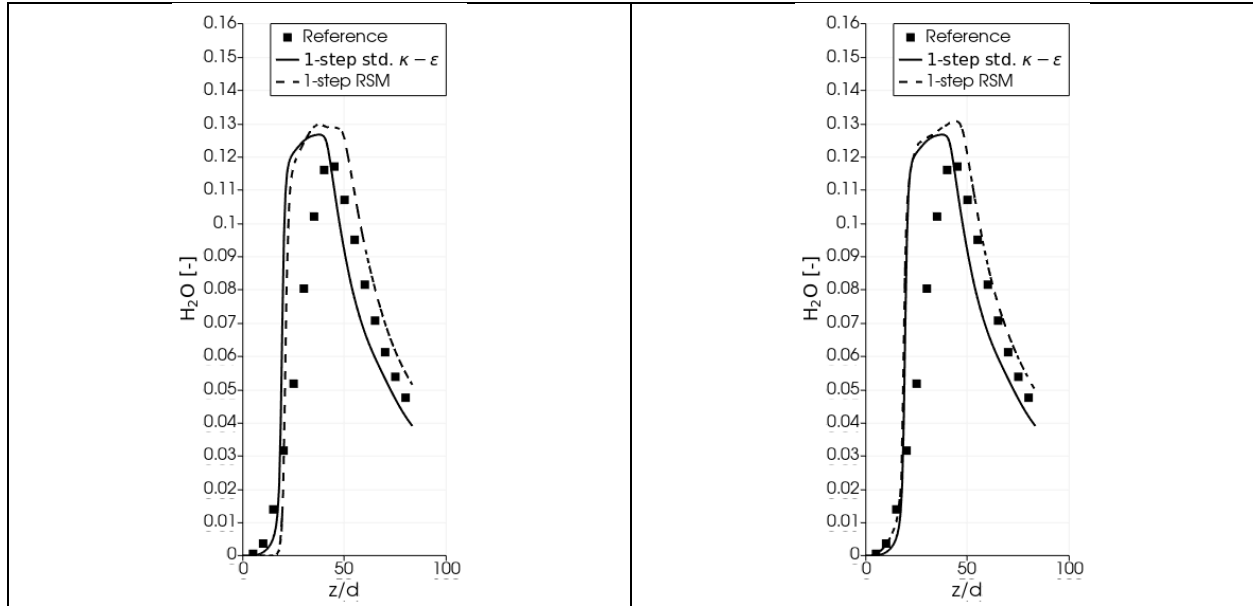


Figure 30: plots of H₂O mass fraction along the symmetry axis: RSM w/o inlet velocity profile (left), RSM w/ inlet velocity profile (right)

GriMech detailed mechanisms

The following sections present the results obtained using the detailed mechanisms of the GriMech family. We present the results obtained from two different versions of the gri3.0 mechanism and the previous gri2.11 version of the detailed mechanism. The first version of the gri3.0 mechanism is distributed with the Sandia D flame tutorial of the openFoam v2012 that has been used throughout the present simulations. This gri3.0 version lacks NO and its related reactions. We present results obtained with this mechanism only because it is distributed with openFoam, so it somehow constitutes a reference. The second version is sourced in CHEMKIN format from the Berkeley gri3.0 website (Berkeley, Berkeley gri3.0, n.d.), and includes 325 reactions and 53 species. The gri2.11 mechanism comprises 277 reactions and 49 species and is available for download in CHEMKIN format from the Berkeley gri2.11 website (Berkeley, Berkeley gri2.11, n.d.).

Gri3.0 mechanism w/ assigned inlet velocity profile

This section reports results obtained with the prescribed inlet velocity profile given in (Workshop, 2003). The following figures offer a comparison of the numerical residual convergence histories and computed results between the standard κ - ϵ and RSM models. We note here that the comparison is not strictly congruent, as we did use the gri3.0 version that did not contain NO reaction for the standard κ - ϵ simulation, and the official gri3.0 version for the RSM.

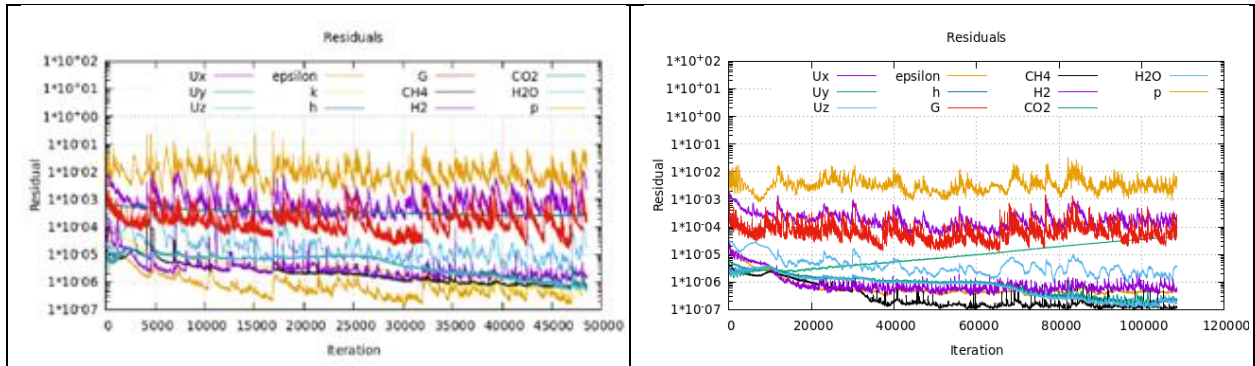


Figure 31: residual convergence history, standard κ - ϵ w/o inlet velocity profile (left), RSM w/ inlet velocity profile (right)

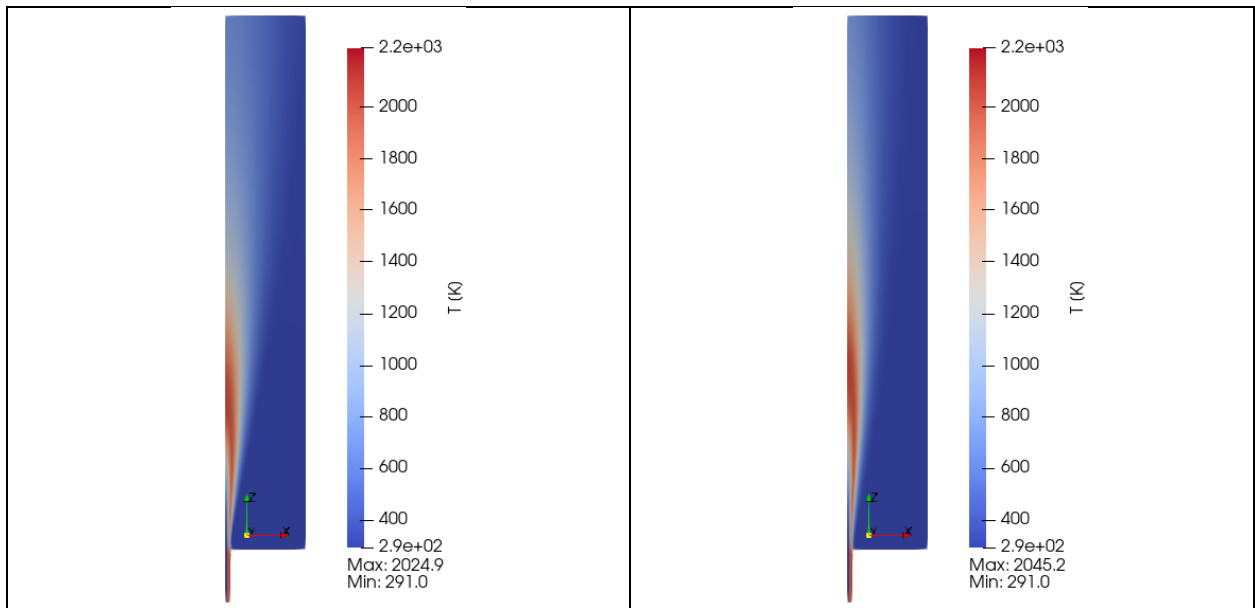


Figure 32: temperature field, standard κ - ϵ w/o inlet velocity profile (left), RSM w/ inlet velocity profile (right)

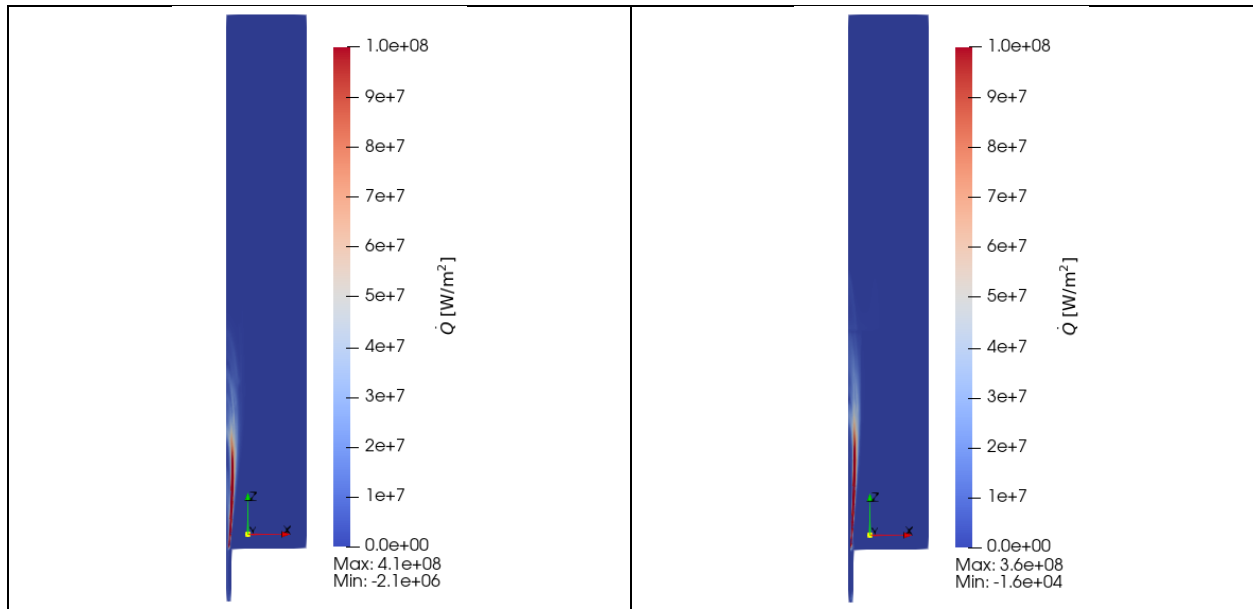


Figure 33: flame front position, identified by \dot{Q} standard $\kappa\text{-}\epsilon$ w/o inlet velocity profile (left), RSM w/ inlet velocity profile (right)

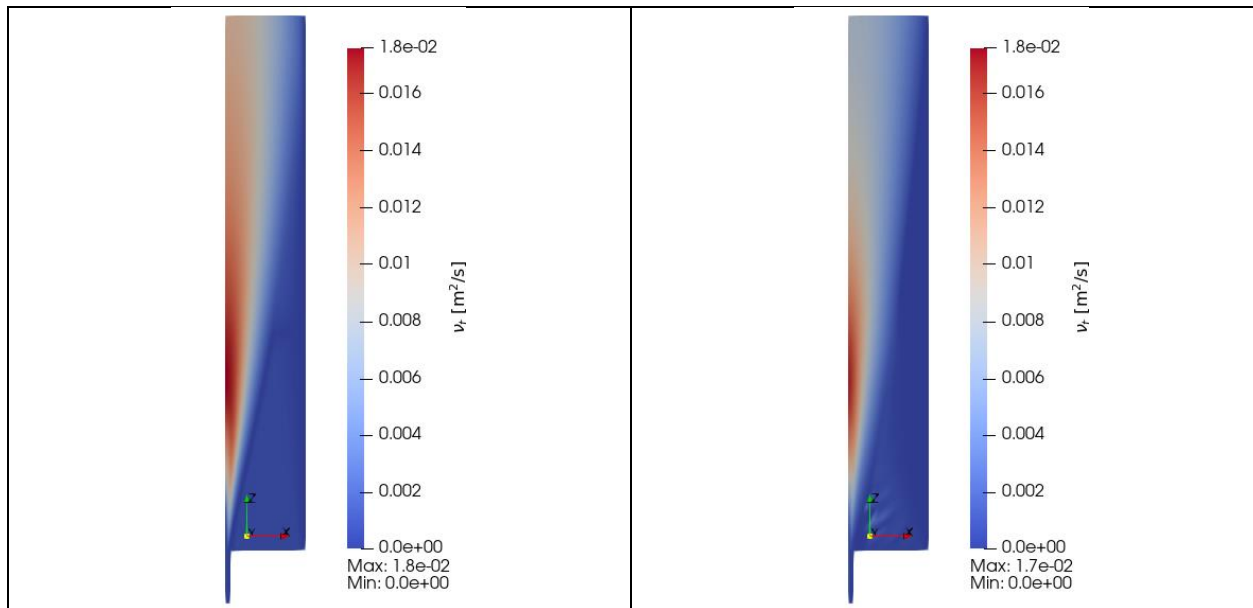


Figure 34: kinematic turbulent viscosity: standard $\kappa\text{-}\epsilon$ w/o inlet velocity profile (left), RSM w/ inlet velocity profile (right)

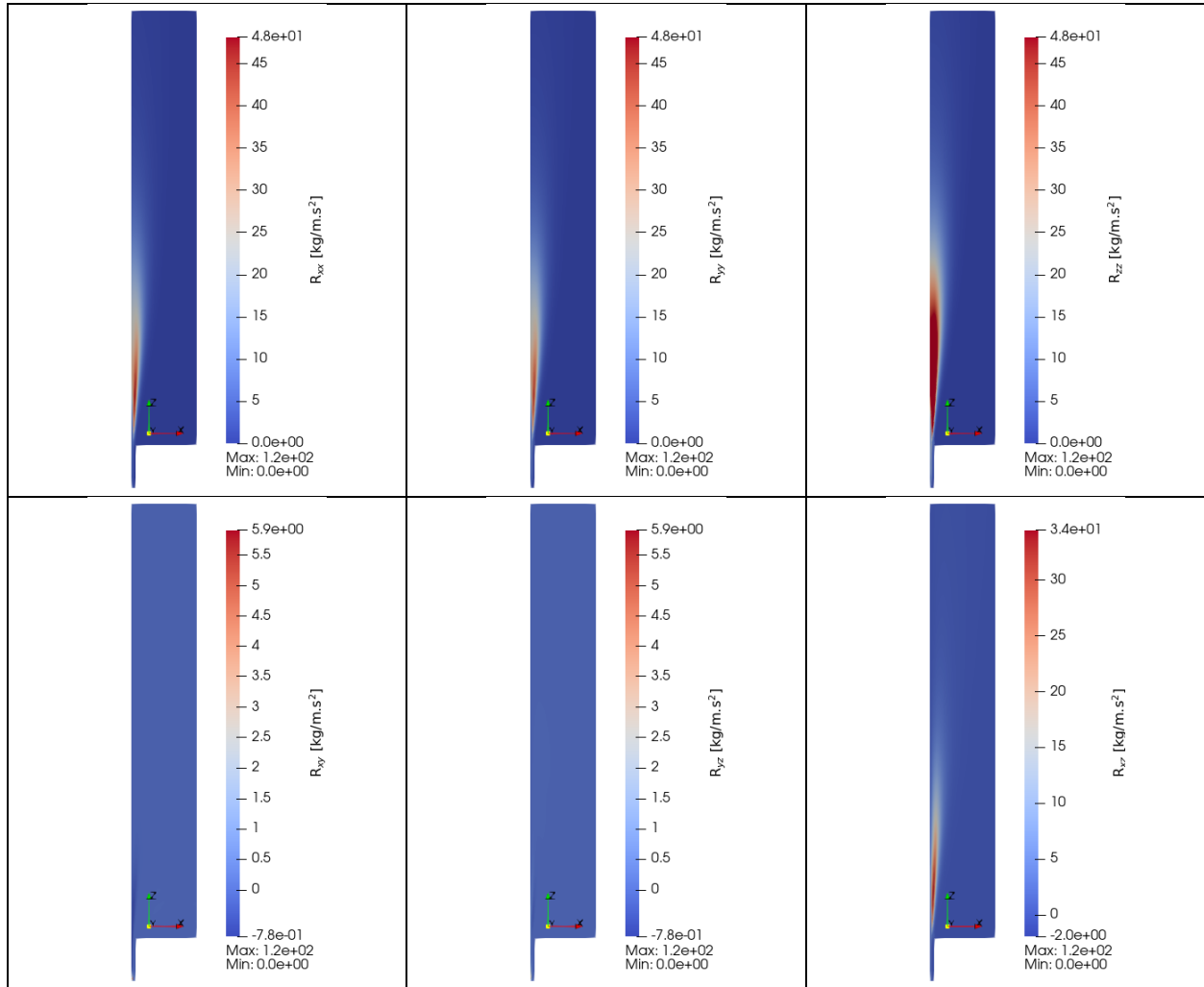


Figure 35: gri3.0, Reynold stress components: top: R_{xx} (left), R_{yy} (center), R_{zz} (right); bottom: R_{xy} (left), R_{yz} (center), R_{zx} (right)

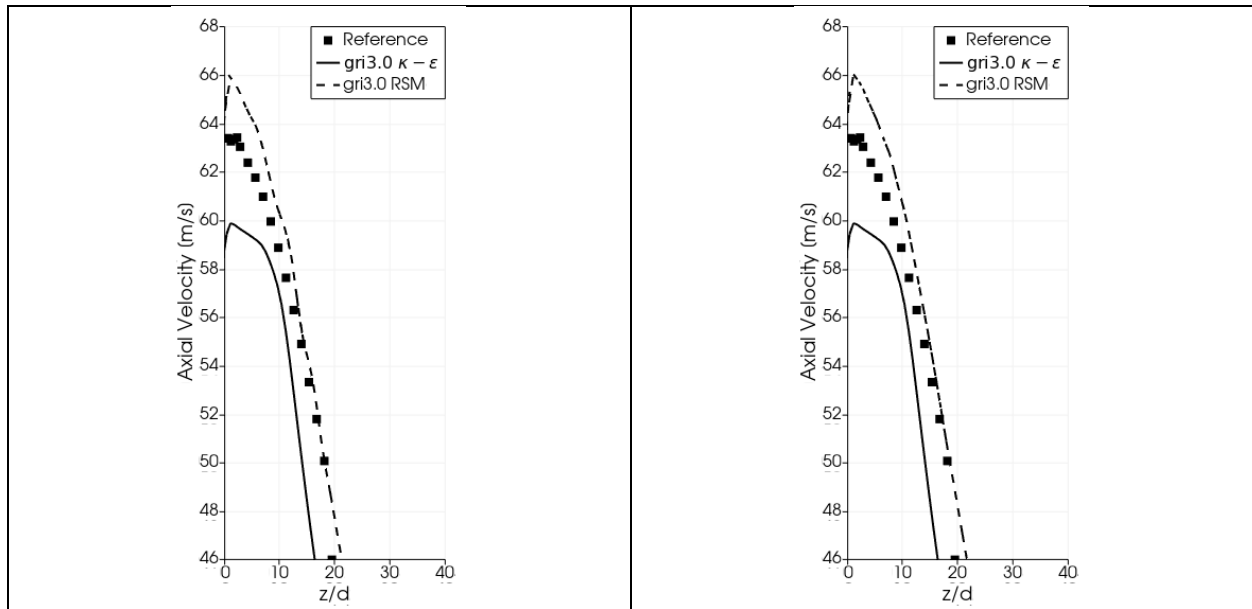


Figure 36: axial velocity component along the symmetry axis (left) and a magnified detail around its maximum value (right)

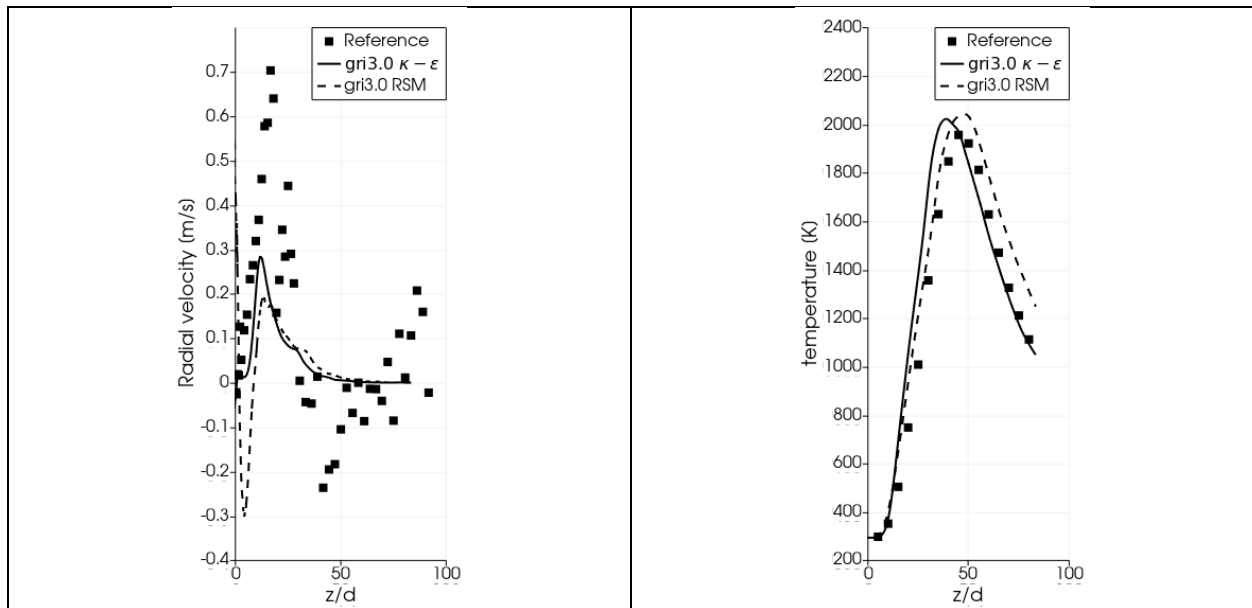


Figure 37: radial velocity component (left) and temperature (right) along the symmetry axis

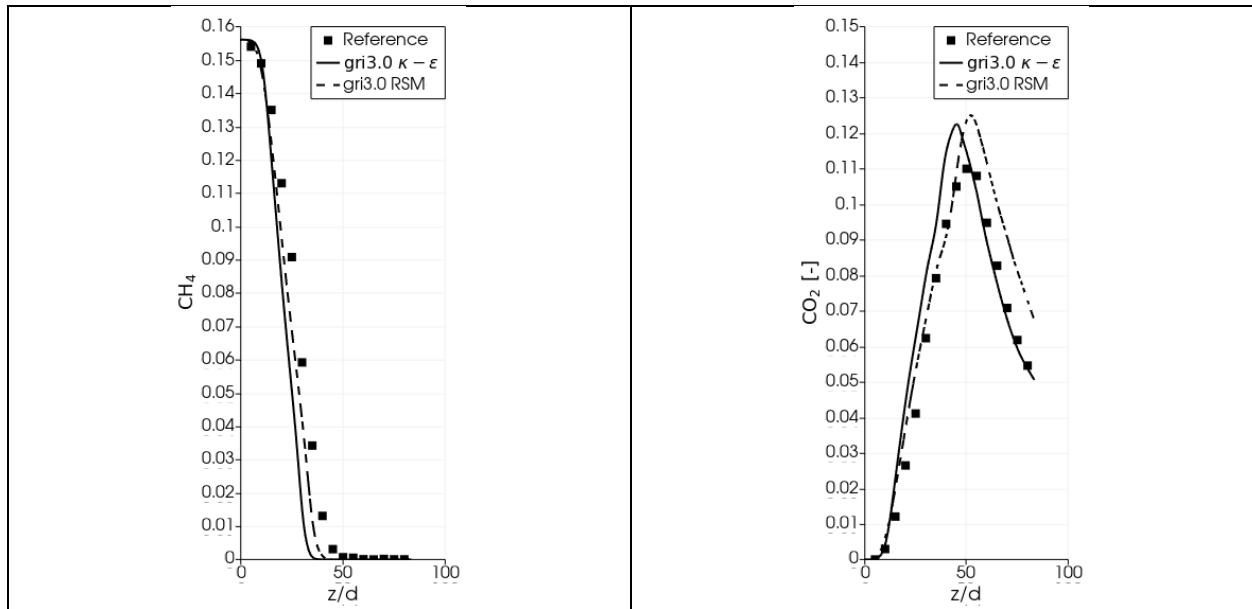


Figure 38: plots of CH_4 (left) and CO_2 (right) mass fraction along the symmetry axis

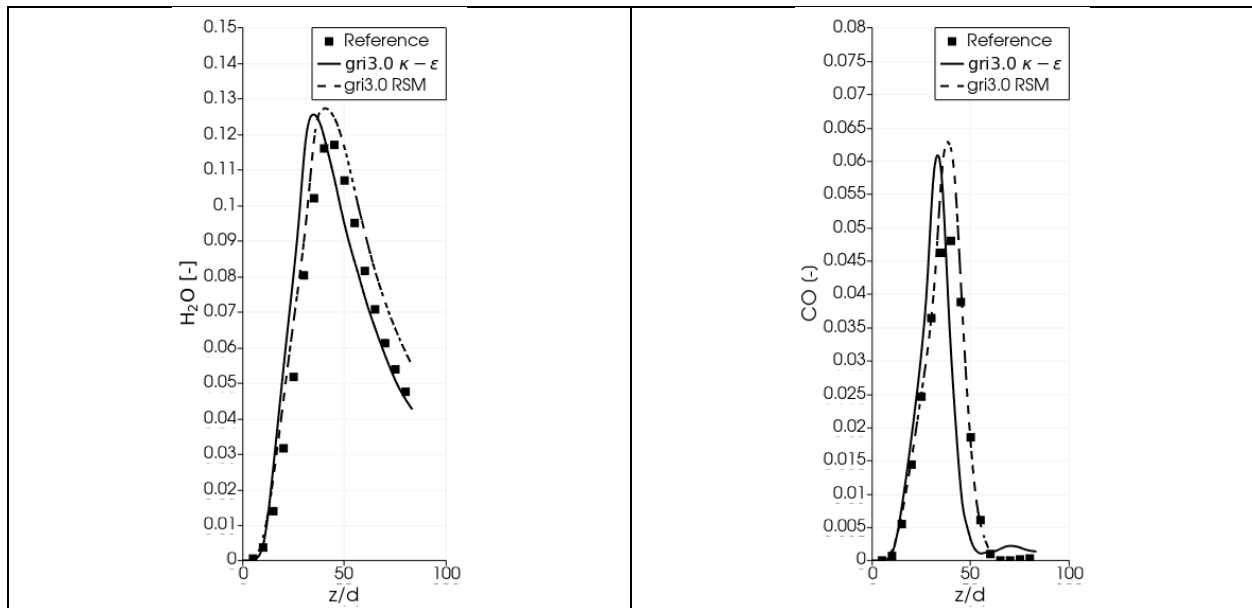


Figure 39: plots of H_2O (left) and CO (right) mass fraction along the symmetry axis

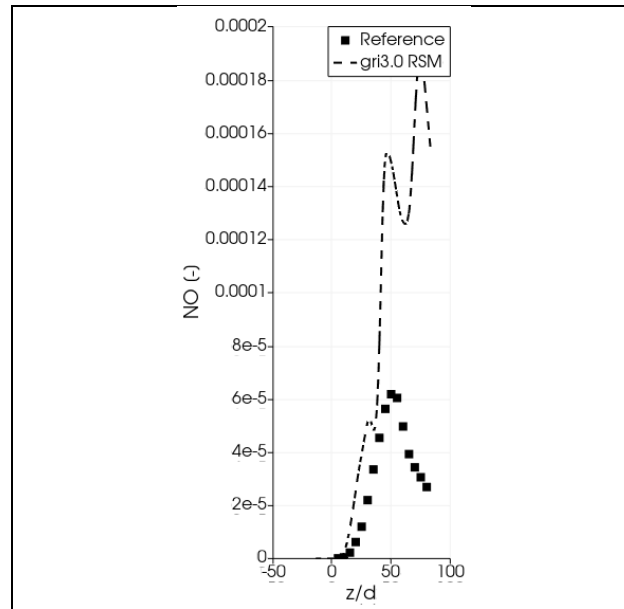


Figure 40: plots of NO mass fraction along the symmetry axis

Gri3.0 vs Gri2.11 mechanism

This section compares results obtained with the gri3.0 (Berkeley, Berkeley gri3.0, n.d.) and the gri2.11 (Berkeley, Berkeley gri2.11, n.d.) detailed mechanisms. The rationale of this comparison is that literature reports a possible tendency of the gri3.0 mechanism to overestimate the NO production (Cantera User Guide, n.d.). We intend to verify this reported behavior in this section.

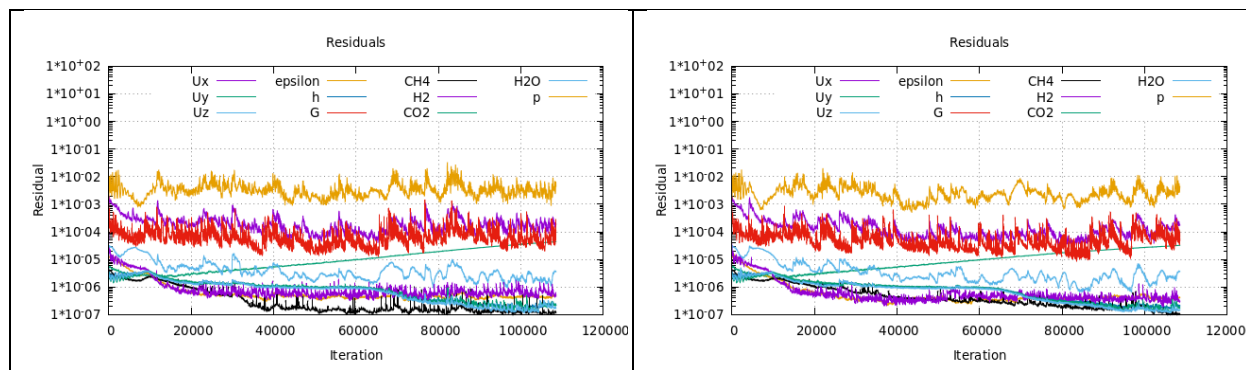


Figure 41: residual convergence history, gri3.0 (left) and gri2.11 (right)

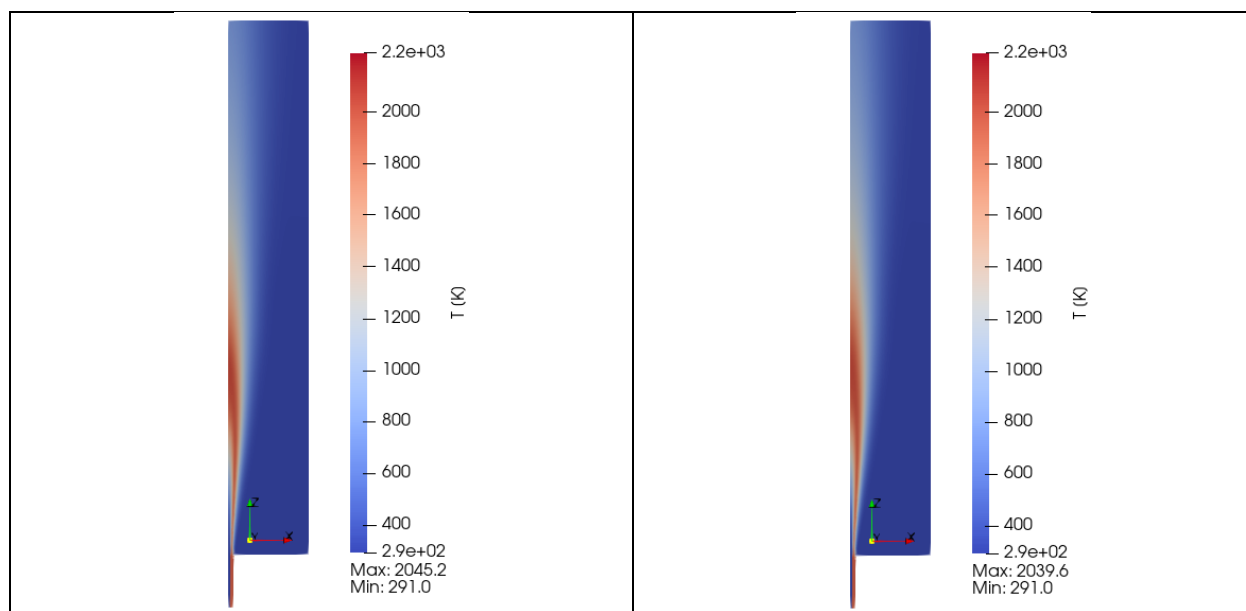


Figure 42: temperature field, gri3.0 (left) and gri2.11 (right)

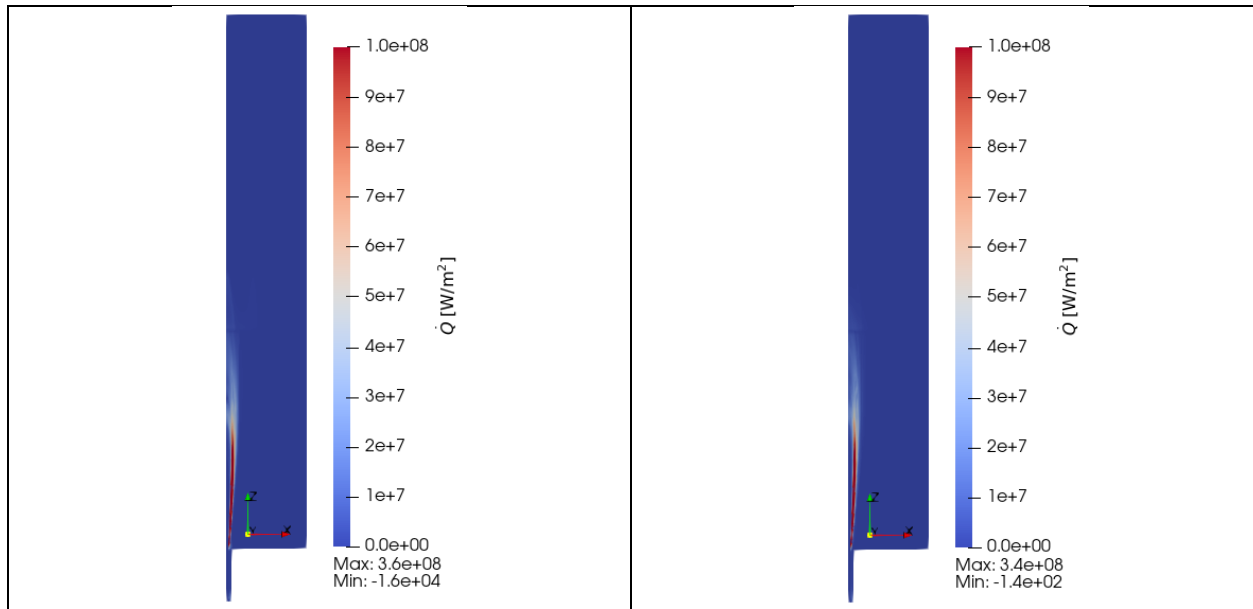


Figure 43: flame front position, identified by \dot{Q} standard, gri3.0 (left) and gri2.11 (right)

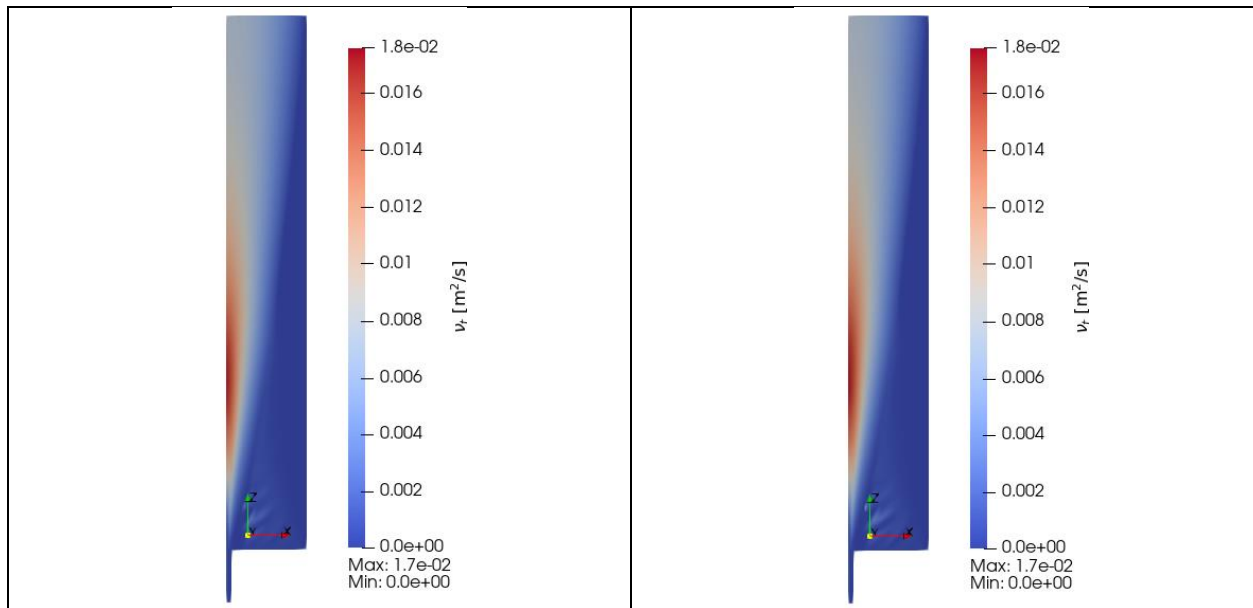


Figure 44: kinematic turbulent viscosity, gri3.0 (left) and gri2.11 (right)

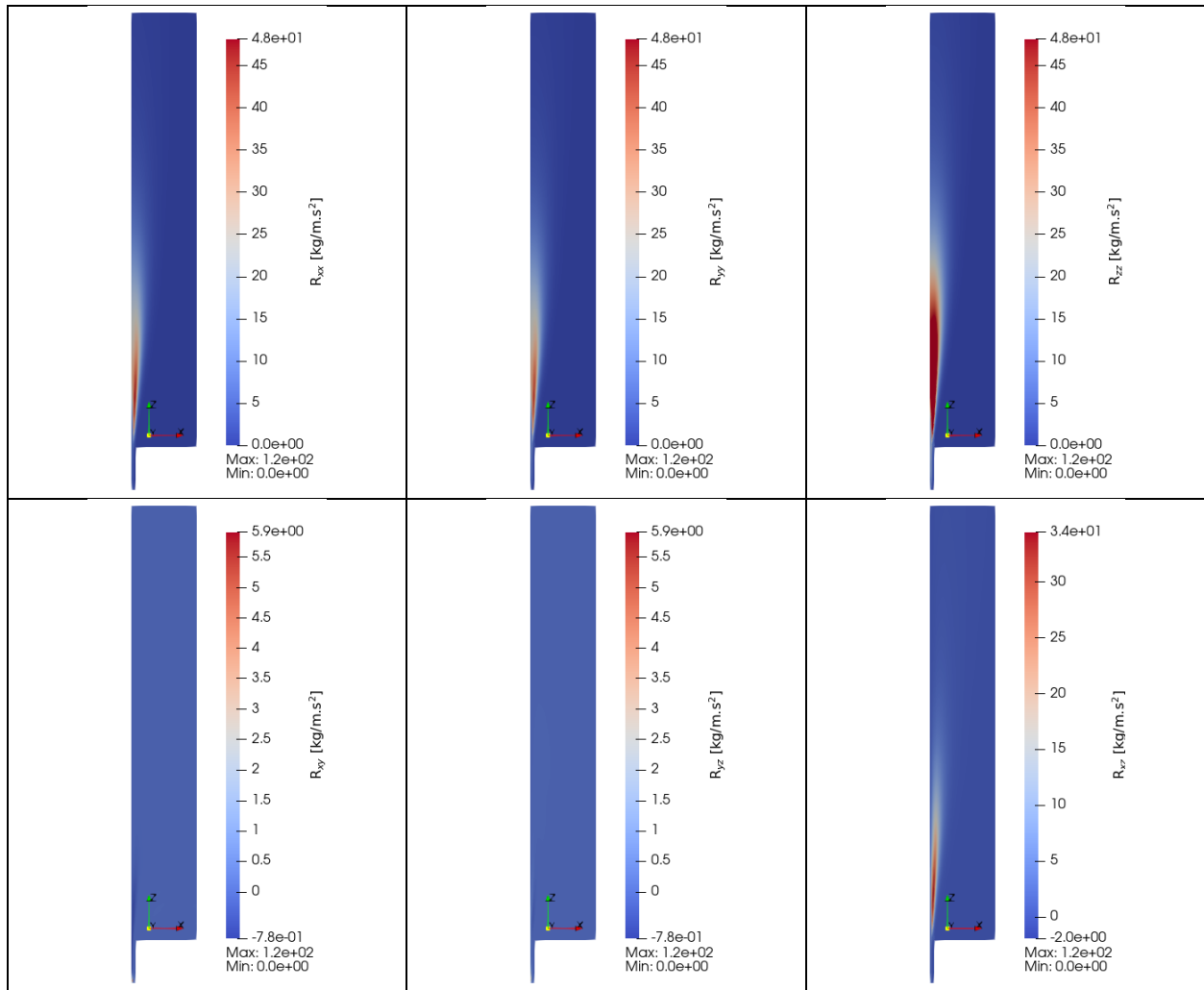


Figure 45: gri3.0, Reynold stress components: top: R_{xx} (left), R_{yy} (center), R_{zz} (right); bottom: R_{xy} (left), R_{yz} (center), R_{zx} (right)

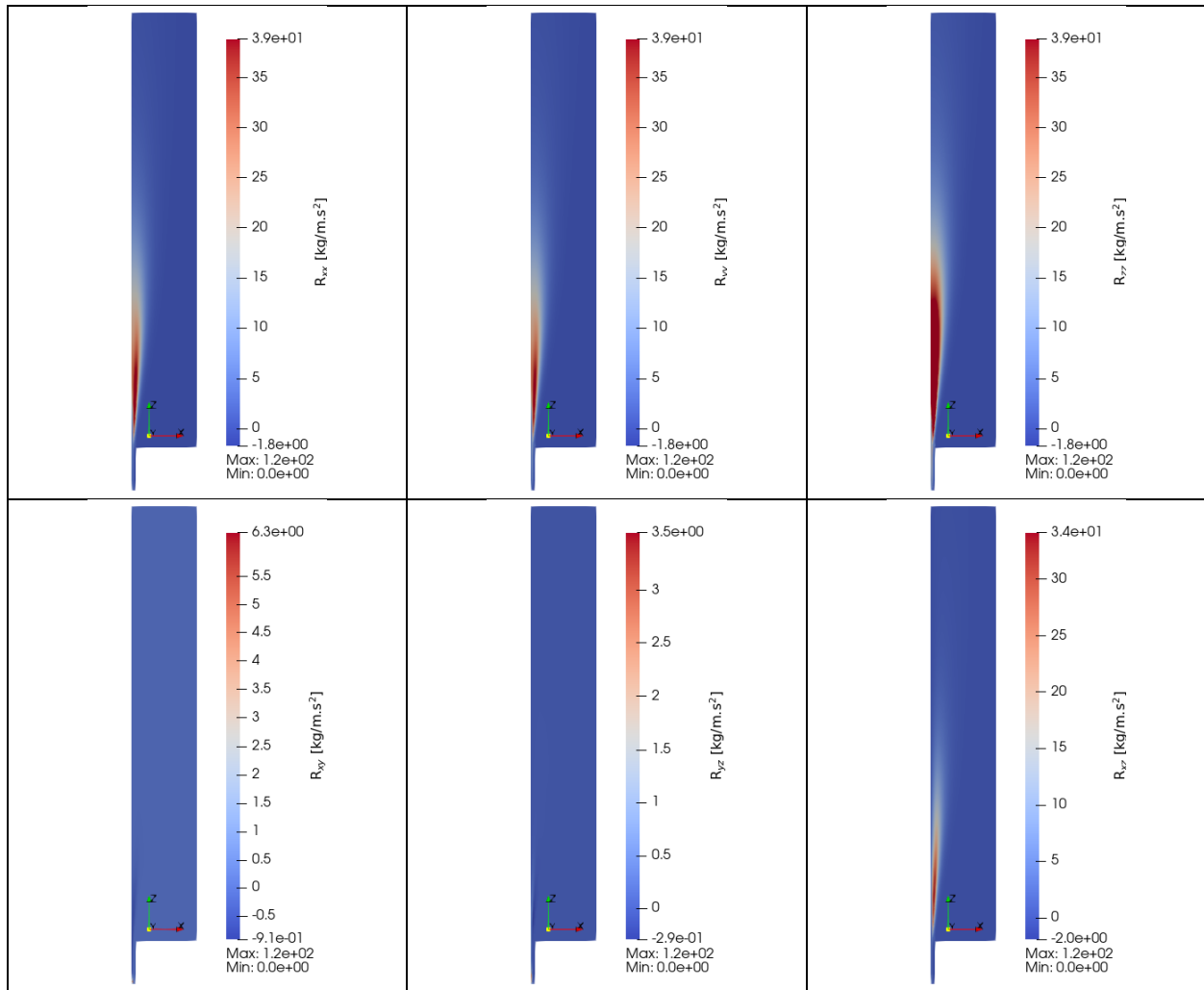


Figure 46: gri2.11, Reynold stress components: top: Rxx (left), Ryy (center), Rzz (right); bottom: Rxy (left), Ryz (center), Rzx (right)

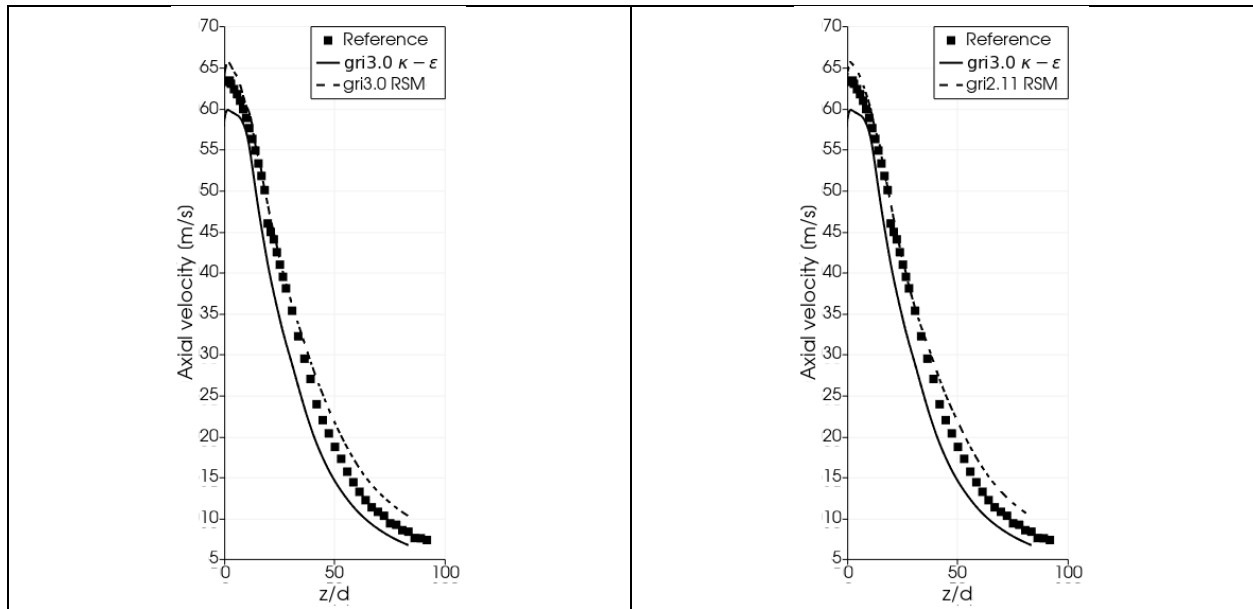


Figure 47: axial velocity component along the symmetry axis, gri3.0 (left) and gri2.11 (right), $\kappa-\epsilon$ solution is kept as a reference

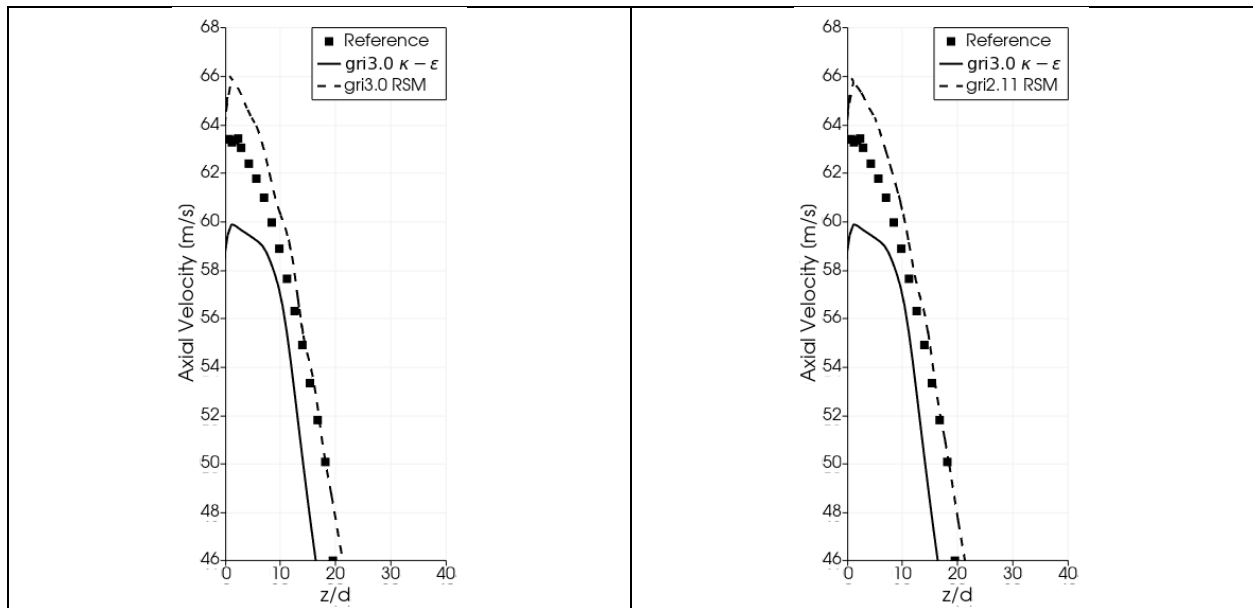


Figure 48: magnified detail around the axial velocity component's maximum value along the symmetry axis, gri3.0 (left) and gri2.11 (right), $\kappa-\epsilon$ solution is kept as a reference

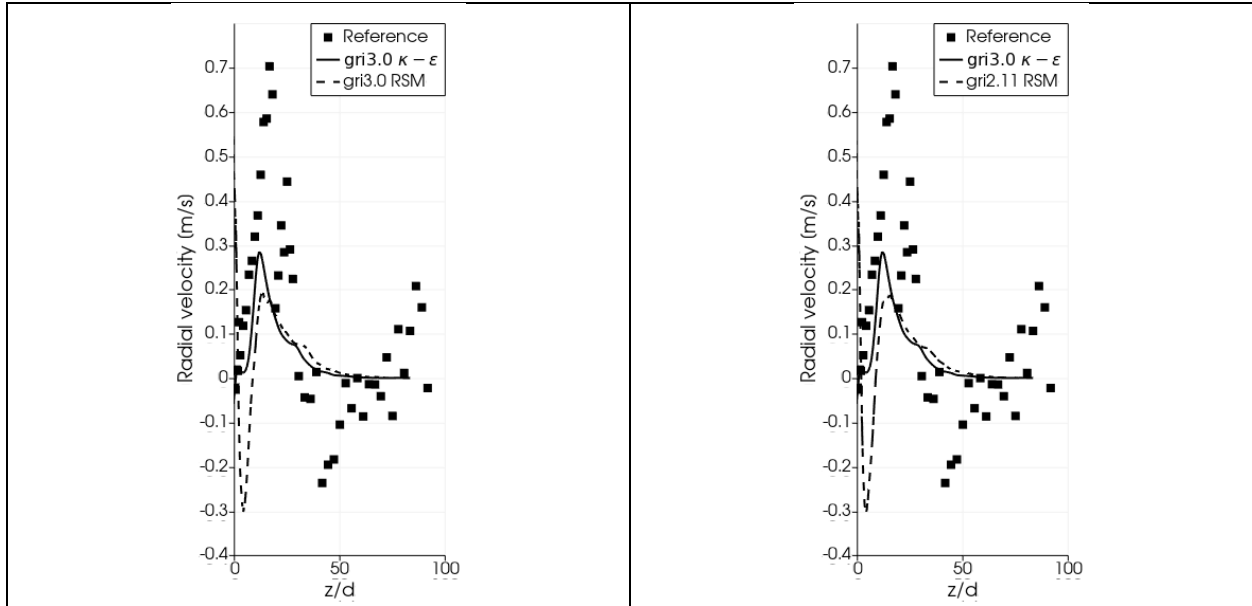


Figure 49: radial velocity component along the symmetry axis, gri3.0 (left) and gri2.11 (right), $\kappa-\epsilon$ solution is kept as a reference

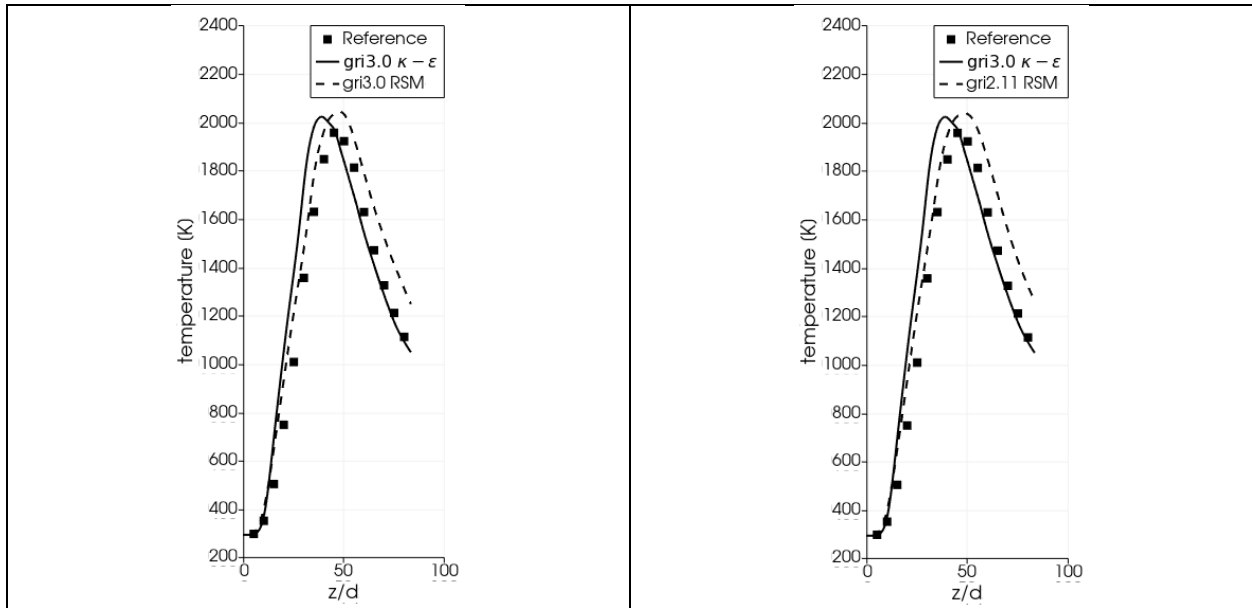


Figure 50: temperature along the symmetry axis, gri3.0 (left) and gri2.11 (right), $\kappa-\epsilon$ solution is kept as a reference

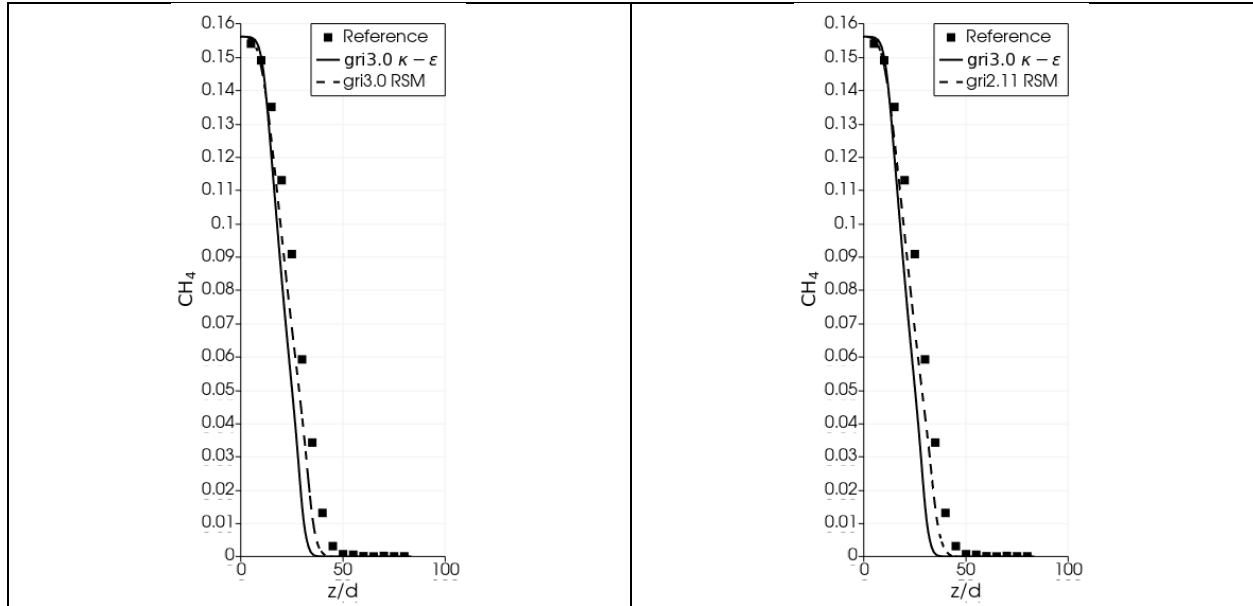


Figure 51: plots of CH_4 mass fraction along the symmetry axis, gri3.0 (left) and gri2.11 (right), κ - ϵ solution is kept as a reference

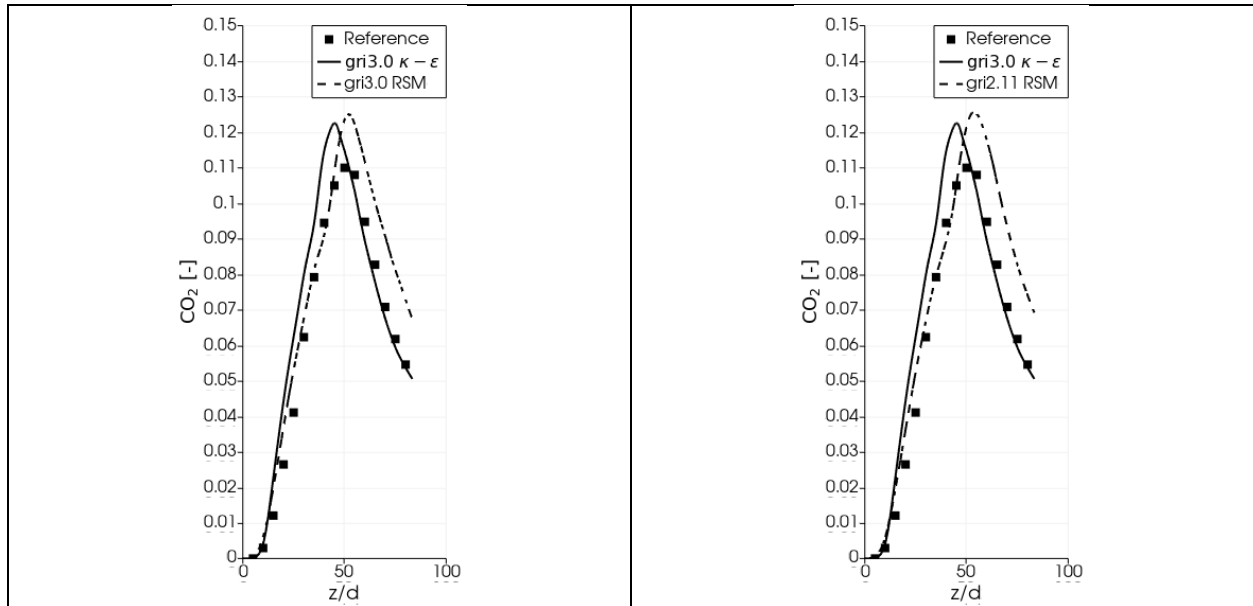


Figure 52: plots of CO_2 mass fraction along the symmetry axis, gri3.0 (left) and gri2.11 (right), κ - ϵ solution is kept as a reference

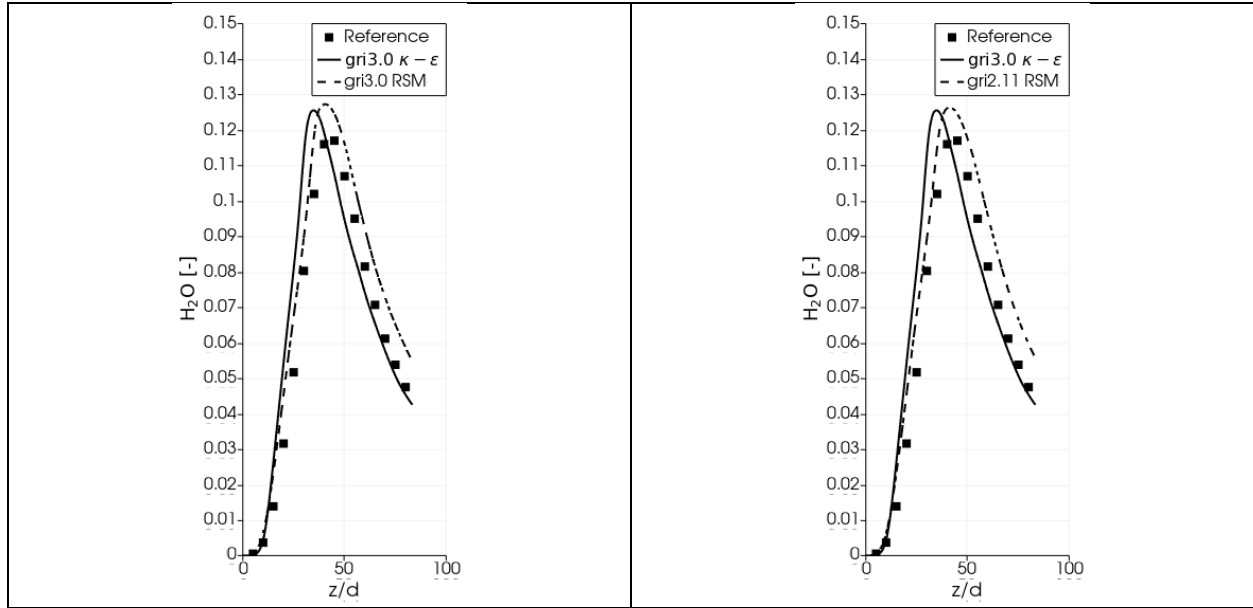


Figure 53: plots of H_2O mass fraction along the symmetry axis, gri3.0 (left) and gri2.11 (right), κ - ϵ solution is kept as a reference

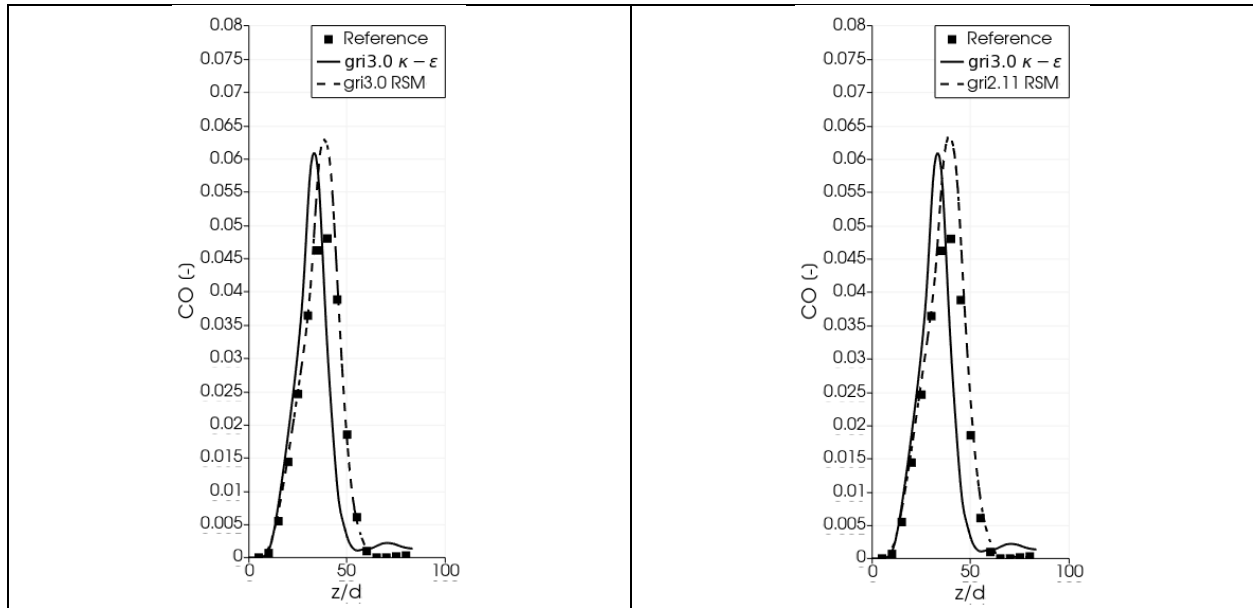


Figure 54: plots of CO mass fraction along the symmetry axis, gri3.0 (left) and gri2.11 (right), κ - ϵ solution is kept as a reference

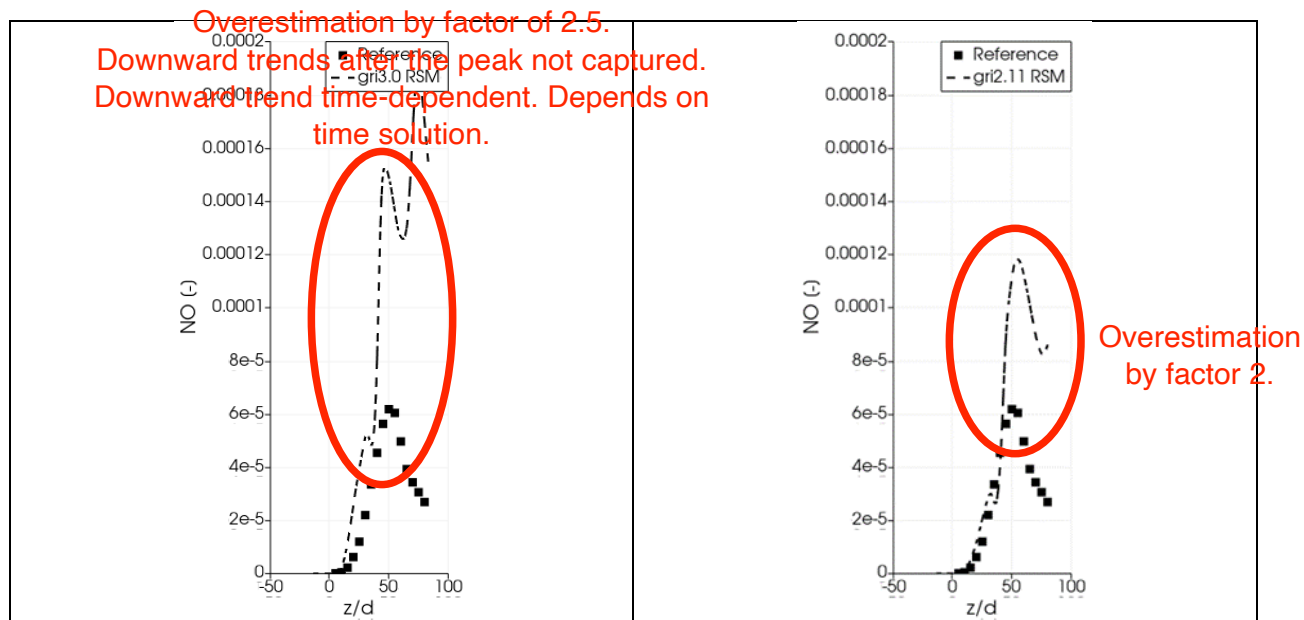


Figure 55: plots of NO mass fraction along the symmetry axis, gri3.0 (left) and gri2.11 (right), κ - ϵ solution is not reported in the figure as the originally used gri3.0 mechanism did not include NO

References

- Berkeley. (n.d.). *Berkeley gri2.11*. Retrieved from <http://combustion.berkeley.edu/gri-mech/new21/version21/text21.html>.
- Berkeley. (n.d.). *Berkeley gri3.0*. Retrieved from <http://combustion.berkeley.edu/gri-mech/version30/text30.html#performance>.
- Cantera User Guide*. (n.d.). Retrieved from <https://chemistry.cerfacs.fr/en/chemical-database/mechanisms-list/1-step-methane-air-mechanism/>
- Jicang Si, G. W. (2020 (34)). Optimization of the Global Reaction Mechanism for MILD Combustion of Methane Using Artificial Neural Network. *Energy Fuels* , 3805–3815.
- Workshop, T. (2003). *Sandia/TUD Piloted CH₄/Air Jet Flames*. Retrieved from <https://tnfworkshop.org/data-archives/pilotedjet/ch4-air/>

APPENDIX

```

/*-----*- C++ -*-----
*\
| ===== |
|
| \ \      /  F i e l d      | OpenFOAM: The Open Source CFD Toolbox
|
| \ \      /  O p e r a t i o n      | Version:  v2012
|
| \ \      /  A n d      | Website:  www.openfoam.com
|
| \ \ /      M a n i p u l a t i o n      |
|
\*-----
*/
FoamFile
{
    version      2.0;
    format       ascii;
    class        volSymmTensorField;
    location     "0";
    object       R;
}
// * * * * *
//
dimensions      [0 2 -2 0 0 0 0];
internalField   uniform (0.0027 0.0027 0.0027 0.0 0.0 0.0);
boundaryField
{
    #includeEtc "caseDicts/setConstraintTypes"
    wallTube
    {
        type      kqRWallFunction;
        value     $internalField;
    }
    outlet
    {
        type      zeroGradient;
    }
    inletPilot
    {
        type      fixedValue;
        //          Rxx  Ryy  Rzz  Rxy Ryz Rxz
        value     uniform (0.77 0.77 0.77 0 0 0);
    }
    inletAir
    {
        type      fixedValue;
        //          Rxx  Ryy  Rzz  Rxy Ryz Rxz
        value     uniform (0.0027 0.0027 0.0027 0 0 0);
    }
    wallOutside
    {
        type      zeroGradient;
    }
}

```

```

}
inletCH4
{
    type          fixedValue;
    //            Rxx  Ryy  Rzz  Rxy  Ryz  Rxz
    value         uniform (7.74 7.74 7.74 0 0 0);
}
frontAndBack_pos
{
    type          wedge;
}
frontAndBack_neg
{
    type          wedge;
}
}
// *****
//

```